The Design and Testing of a Frequency-Tunable Mechanically Actuated Microstrip Patch Antenna

Reena Al-Dahleh

Department of Electrical & Computer Engineering

University of Manitoba

Winnipeg, Canada

A thesis submitted to

the Faculty of Graduate Studies

in partial fulfillment of

the requirements for the degree of

Masters of Science

THE UNIVERSITY OF MANITOBA

FACULTY OF GRADUATE STUDIES

*****

COPYRIGHT PERMISSION PAGE

THE DESIGN AND TESTING OF A FREQUENCY-TUNABLE MECHANICALLY ACTUATED MICROSTRIP PATCH ANTENNA

BY

REENA AL-DAHLEH

A Thesis/Practicum submitted to the Faculty of Graduate Studies of The University of Manitoba in partial fulfillment of the requirements of the degree of

Master of Science

Acknowledgments

I would first and foremost like to thank Dr. Cyrus Shafai and Dr. Lot Shafai for their help and support throughout the research period. Their guidance through this thesis has been invaluable, and their knowledge and experience have been a great resource for me to explore. I would like to really thank Dr. Soliman for agreeing to be my external advisor on such short notice, his feedback is truly appreciated.

I would also like to extend my thanks to Brad Tabachnik and Allen Symmons for their constant technical assistance, and to Shelly Girardin for her continuous support and help. Also, a special thanks to my friends and peers who have provided me with support and advice.

Last but not least, I would like to express my gratitude to my parents for supporting me throughout this journey. They have provided me with the backbone to achieve one of the many goals I have set in life, and continue to with endless love and support.

Abstract

There is a rising need for multiple frequency and broadband antennas in today's communications systems. A frequency-tunable single microstrip patch antenna element with a stacked air-glass substrate is presented in this thesis. Adjusting the air-gap height between the patch and ground plane varies the antenna's effective dielectric constant, resulting in a shift in resonant frequency while maintaining a low dielectric constant. Ensemble simulations and experimental results are presented for the two models built: the bulk-machined and micromachined model. Microstrip patch antennas of frequencies ranging between 5 GHz to 18.9 GHz exhibited frequency shifts of up to 5 % for the bulk-machined model. Implementing the 18.9 GHz antenna in a micromachined model, a resonant frequency shift of 1.05 GHz was observed (almost 5.6 %).

Table of Contents

List of Figures

List of Tables

Chapter 1

Introduction

1.1 Problem Definition

The current trend in commercial and government communication systems has been to develop low cost, light weight, low profile antennas that are capable of maintaining high performance over a large spectrum of frequencies (broadband antennas). Due to their structural simplicity, low manufacturing cost and compatibility with MMIC (Monolithic Microwave Integrated Circuits), microstrip patch antennas (MPAs) are becoming more prominent in today's antennas field. These advantages have led to the implementation of microstrip antennas in satellite, radar, military and biomedical applications. However, despite their many advantages, these planar antennas have some limitations when implemented on high dielectric substrates such as their innately narrow bandwidth, lower gain (~ 6 dB) and poor power handling capability (~100 W) [1].

To obtain an efficient, broadband antenna, electrically thick substrates are required. However, when the substrate thickness increases, surface waves are excited resulting in the loss of a substantial amount of radiated power [1]. Thick substrates also introduce problems and complexities associated with the antenna's feed system. Furthermore, higher-order cavity modes with fields depending on the substrate thickness may develop, introducing distortions in the pattern and impedance characteristics [2]. MPAs printed on thin substrates for lower power loss posses a narrow bandwidth due to

the intrinsic high quality-factor resonating cavity present beneath the patch, i.e. the substrate. Another design issue faced is the ability to tune a single MPA's operating frequency to several adjacent channels. However, since the resonant frequency is determined primarily by the substrate permittivity, and the shape and size of the patch, it is evident that to change the resonant frequency would require a new antenna element. Therefore, it is necessary to develop more sophisticated methods to enhance the absolute bandwidth and frequency agility of MPAs, and a great deal of research has been devoted to this as discussed in the following section.

1.2 Literature Review

During the last decade, an extensive amount of research has been dedicated to increasing the frequency agility of MPAs. The concept of bandwidth and frequency agility performance is illustrated in Figure 1.

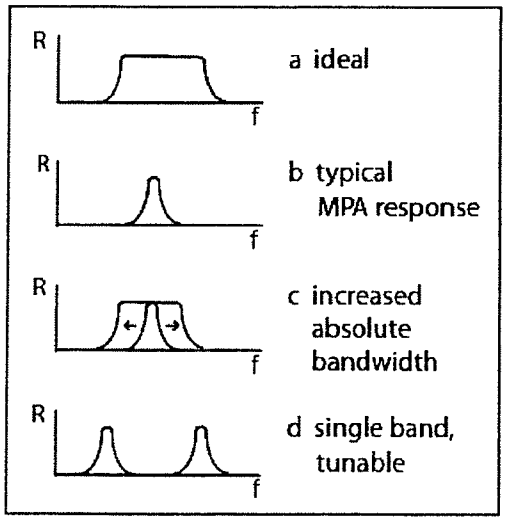

Figure 1.1: *Various frequency response characteristics [2].*

The ideal response desired in today's communication systems is depicted in Figure 1(a), in comparison to a typical MPA frequency response in Figure 1(b). In terms of frequency agility, a single-band tunable antenna with a frequency response illustrated in Figure 1(c) can serve this purpose. There were several methods proposed to enhance MPA frequency agility and bandwidth including loading the patch with components such as Varactor diodes, optically controlled PIN diodes and shorting pins [2]. However, implementing these methods complicate the antenna design and sacrifice its monolithic geometry. A simpler method proposed by Dahele for a coaxial probe-fed patch antenna is shown in Figure 1.2 [3]. Different height spacers are manually introduced, adjusting the air-gap thickness between the substrate and ground plane, and resulting in a change in the effective permittivity, and hence a shift in resonant frequency.

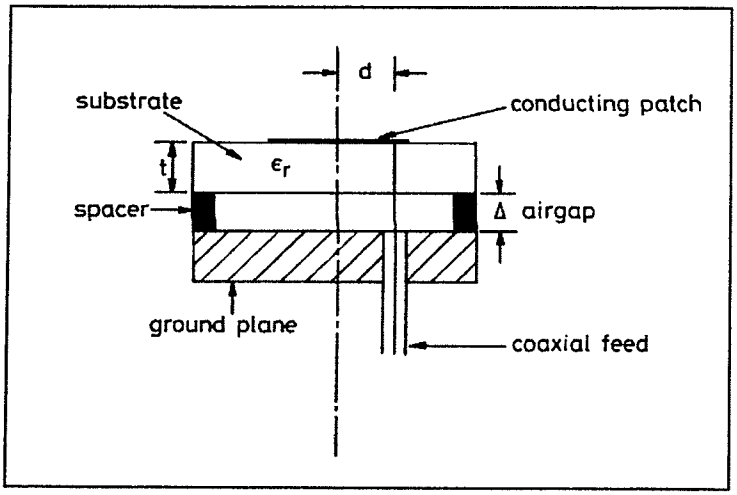

Figure 1.2: *Geometry of a microstrip antenna with air-gap proposed by Dahele [3].*

1.3 Thesis Objectives

The main objective of this thesis is to introduce for the very first time a machined MPA that is mechanically tunable to resonate at several frequencies. Two models of this proposed antenna are designed: a bulk and a micromachined model. The bulk-machined model is a larger scale model designed to confirm the behaviour predicted by simulations run in Ansoft's Ensemble 8.0. The micromachined model utilizes a micromachined corrugated copper membrane to vary the air-gap height between the patch and ground plane. Thus, the effective dielectric constant is altered, resulting in a shift in frequency. The advantages of implementing MEMS actuators over semiconductors include reduced element size and volume with ease of mechanical actuation. This thesis will then present and compare the experimental results with the simulation results obtained.

1.4 Organization

Chapter two provides some background on MPAs, focusing on antenna operation, and the basic design parameters used to characterize their performance. Also presented are the fabrication processes used for MEMs design including photolithography, chemical etching, copper evaporation and XeF_2 release etching. The mathematical modeling of the corrugated copper membrane is also briefly described in this chapter. Chapter three describes and compares the Ensemble software simulation results obtained for the initial three models of the adjustable air-gap MPA considered. Also presented and analyzed in this chapter are the simulation results obtained for the antenna model chosen to resonate at 5 GHz, 10 GHz and 20 GHz.

Chapter four discusses the design and fabrication of the bulk model, comparing the simulated results with the measured results. Dimensions as well as material properties are presented in detail. The following chapter then presents the design, fabrication and results obtained for the micromachined model. The measured data from the micromachined antenna is then compared with the simulated data. Finally, chapter six provides concluding remarks on the overall performance along with suggestions for improvement and future work.

Chapter 2

Background Theory

Decades of research have concluded that the performance and operation of a microstrip antenna is driven mainly by the geometry of the printed patch, and the material characteristics of the substrate onto which the antenna is printed. Therefore, it is conceivable that with proper manipulation of these parameters, improved antenna performance in terms of bandwidth and frequency agility can result. The following sections discuss how MPAs operate, and the parameters that affect their performance. In addition, a brief description of the micromachining processes used for the deposition, patterning and removal of material is presented. Finally, the mathematical model of a corrugated membrane will be briefly described.

2.1 Antenna Background Theory

The MPA is of simple planar geometry and its operation is very easy to understand. The following sections will provide some background on the patch antenna's operation, design parameters of interest, and feeding technique.

2.1.1 MPA Operation

Figure 2.1 shows a conventional microstrip line-fed MPA antenna, linearly polarized in the y direction, that consists of a ground plane and a radiating patch separated by a dielectric medium, referred to as the substrate, with a dielectric constant ε_r of height h.

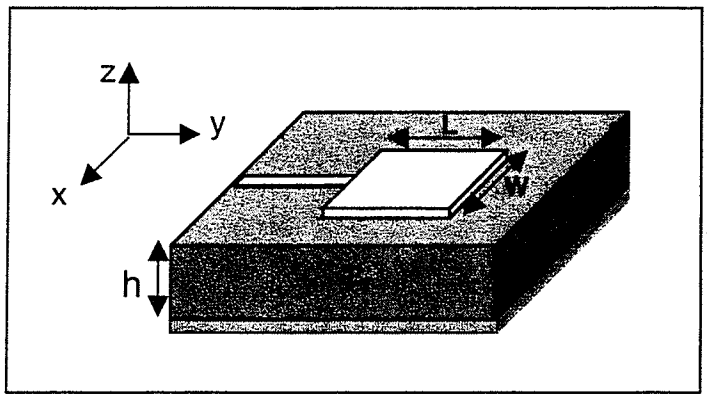

Figure 2.1: *The geometry of a standard microstrip antenna.*

The upper conducting patch is the source of radiation, where electromagnetic energy fringes off the edges of the patch and into the substrate. The perfectly reflecting ground plane bounces the energy back through the substrate into free space. The radiating patch may be rectangular, square, circular, ring, elliptical, triangular or any other configuration. In most practical applications, patch antennas are rectangular and circular because of the ease of analysis and low cross polarization radiation characteristics [4]. The rectangular patch radiates and behaves as a one-dimensional resonator when its width is set to a half-wavelength ($\frac{\lambda_{eff}}{2}$).

The antenna can be analytically modelled, using the transmission-line model or the cavity model, to obtain a better understanding of its behaviour. The transmission line model of the microstrip antenna consists of two radiating slots, represented by admittance, and separated by a low-impedance Z_c transmission line of length $\frac{\lambda_{eff}}{2}$. The feedline is connected in parallel with the main transmission line in a position corresponding to the location of the connection to the patch. The input impedance of the patch depends on the distance from the edges of the patch to the feed point.

In the cavity model, a patch antenna is represented as a dielectric loaded cavity. The cavity is formed via a substrate that is truncated on the top and bottom by two perfectly conducting electric boundaries – the patch and ground plane. The sidewalls are perfectly conducting magnetic boundaries that are determined by the dimensions of the patch. Therefore, the electric field lines contained within the substrate (between the patch and ground plane) are propagating perpendicular to the conducting walls, as required by Maxwell's equations.

The electric field present in the dielectric substrate is highly dependent on the thickness of the substrate, h, as illustrated in Figure 2.2. For a small h, the electric field is normal to the patch, whereas for a large h, the fringing fields are more prominent at the edges of the patch making the patch appear longer, also known as the effective length L_e $(L_e = L + 2\Delta L)$.

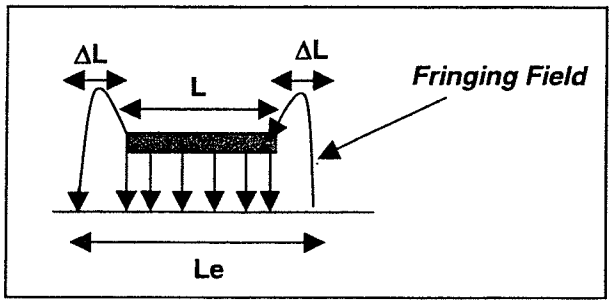

Figure 2.2: *Fringing effects on a patch antenna's length.*

The incremental length can be found from equation (2.1):

$$\Delta L = \frac{0.412h\left[(\varepsilon_e + 0.3)\left(\frac{W}{h} + 0.264\right)\right]}{\left[(\varepsilon_e - 0.258)\left(\frac{W}{h} + 0.8\right)\right]} \qquad (2.1)$$

which depends on the effective dielectric constant, ε_e. The effective dielectric constant is highly dependent on the substrate height h, substrate relative constant ε_r, and patch width W as shown in equation (2.2).

$$\varepsilon_e = \frac{\varepsilon_r + 1}{2} + \frac{\varepsilon_r - 1}{2}\left[1 + 12\frac{h}{W}\right]^{-\frac{1}{2}} \tag{2.2}$$

2.1.2 Antenna Parameters

The patch's effective length and effective permittivity determine the resonant frequency and are critical design parameters because of the patch's inherently limited bandwidth. The resonant frequency of a microstrip patch antenna can be found using equation (2.3).

$$f_r = \frac{c}{2(L + 2\Delta L)\sqrt{\varepsilon_e}} \tag{2.3}$$

The bandwidth (BW) of an antenna is defined as the range of frequencies on either side of a centre frequency (usually resonant frequency), where the antenna characteristics are within an acceptable value of those at the center frequency [1]. The input impedance of a patch antenna is frequency dependent, thus limiting the frequency range over which the element can be matched to its feed line. Therefore, the half-power BW is most often defined in terms of the relative frequency range over which the antenna's VSWR (voltage standing wave ratio) is less than 2. This is mathematically expressed as:

$$BW = \frac{VSWR - 1}{Q_t \sqrt{VSWR}} \tag{2.4}$$

where the quality factor, Q_t, quantifies all the antenna losses including: radiated losses (Q_{rad}), conduction losses (Q_c), dielectric losses (Q_d) and surface wave losses (Q_{sw}). The expression for the Q factor is represented by equation (2.5).

$$\frac{1}{Q_t} = \frac{1}{Q_{rad}} + \frac{1}{Q_c} + \frac{1}{Q_d} + \frac{1}{Q_{sw}} \tag{2.5}$$

For a very thin substrate, surface wave losses induced along the patch's surface are negligible. The MPA's bandwidth can also be defined as the ratio of the antenna's resonance frequency, f_r, and the frequency band over which the reflection coefficient (S_{11}) remains below –10 dB:

$$Q_t = \frac{f_r}{\Delta f} \tag{2.6}$$

Using the cavity model approach, the total radiated fields can be found at far field and are given by the equations (2.7) and (2.8). The frequencies and the input impedance are determined by considering the excitation of the cavity.

The tangential electric field on the sidewall boundaries is determined and then replaced by an equivalent magnetic current on a perfect electric conducting boundary. The radiation pattern produced by this current is then determined assuming the cavity is surrounded by free space.

$$E_\theta = \left[\frac{jkWV_0}{\pi r} e^{-jkr} e^{j(X+Y+Z)}\right] \cos(\Phi) \left[\frac{\cos(X)\sin(Y)}{Y}\right] \tag{2.7}$$

$$E_\varphi = \left[\frac{jkWV_0}{\pi r} e^{-jkr} e^{j(X+Y+Z)}\right] \cos(\theta)\sin(\Phi) \left[\frac{\cos(X)\sin(Y)}{Y}\right] \tag{2.8}$$

where V_0 is the excitation voltage applied at the feed and the variables X, Y, and Z are expressions in terms of the antenna parameters shown in the equations below [3].

$$X = \left[\frac{kL_e}{2}\right] \sin(\theta)\cos(\Phi) \tag{2.9}$$

$$Y = \left[\frac{kW}{2}\right] \sin(\theta)\sin(\Phi) \tag{2.10}$$

$$Z = \left[\frac{kh}{2}\right] \cos(\theta) \tag{2.11}$$

2.1.3 Antenna Feeding Technique and Modelling

There are several methods used to feed microstrip antennas; a microstrip line, coaxial probe, aperture coupling and proximity coupling. The microstip line feed method shown in Figure 2.3 uses direct contact with the patch to produce excitation and is known as a direct contact feed. It is one of the simplest feeds to model, and it enables the designer to manipulate several parameters by adjusting the contact point (excitation point). These parameters include: the impedance match between the feed and antenna, polarization, mode of operation, and the excitation frequency. A main disadvantage of direct contact feeds is their very narrow bandwidth. These feeds, whether coaxial or microstrip, are "matched" to specific impedances (typically 50Ω) over a select range of frequencies. Operation outside this range degrades antenna performance due to the inherent mismatch between the antenna and the feed.

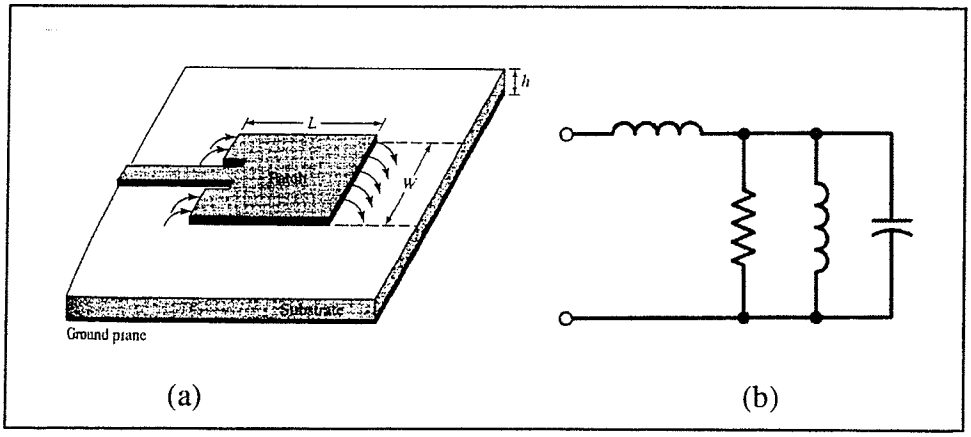

Figure 2.3: *(a) Microstrip line-fed MPA and (b) its equivalent circuit diagram [1].*

In the equivalent circuit, an RLC circuit represents the patch, where the resistance R corresponds to the losses associated with the conductors and substrate.

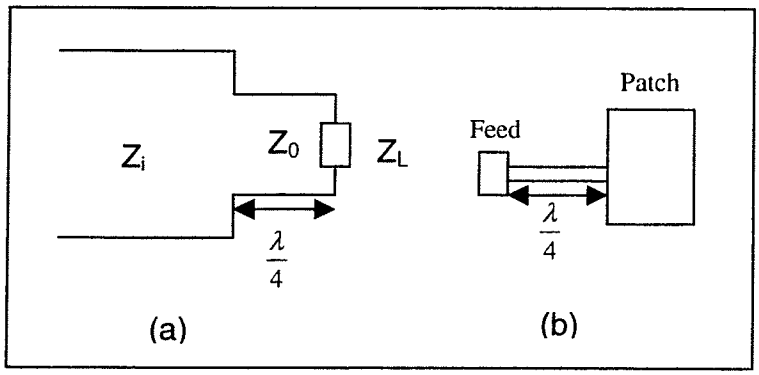

Figure 2.4: *Load matching using a quarter-wave transformer: (a) circuit diagram, and (b) antenna layout.*

Selecting the type of feed technique is governed by the efficient transfer of power between the radiating structure and feed structure, that is, impedance matching between the two [4]. A quarter-wave transformer shown in Figure 2.3 is typically used to match the patch element (load impedance Z_L) to a typical 50Ω connection (input impedance Z_{in}) using equation (2.12).

$$Z_0 = \sqrt{Z_{in} Z_L} \qquad (2.12)$$

2.2 Micromachining Background Theory

The processes to create miniaturized actuators and MEMS devices including deposition, patterning and removal of material in micromachining are similar to those originally used in IC fabrication. Micromachining consists of fabrication procedures subdivided into two kinds: bulk micromachining and surface micromachining. Bulk micromachining refers to removing a large, or bulk, portion of the wafer, whereas, surface micromachining refers to the fabrication processes that occur on the wafer's surface. This section describes the processes used for material deposition, patterning and removal performed on either the bulk and/or surface of the wafer.

2.2.1 Deposition Processes

There are several methods used to deposit thin films that can be of metallic or non-metallic nature. These surface machining methods include: spin-on, thermal evaporation, sputtering, and chemical vapour deposition. The type of deposition process used depends on the type of film material. The photoresist, a photoactive polymer used for patterning, is typically spun onto the wafer. For thin metallic films (up to a thickness of approximately 2 μm), thermal evaporation is typically used at the University of Manitoba.

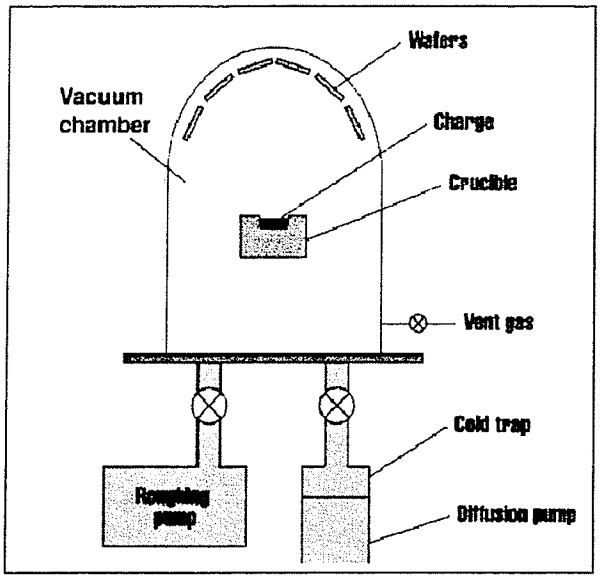

Figure 2.5: *Evaporation chamber set-up.*

Thermal evaporation, also referred to resistive evaporation, uses an electrically heated filament of the desired metal or a refractory metal "boat" or crucible containing the desired metal at the bottom of a chamber [5]. Once the chamber is pumped down to 10^{-9} to 10^{-10} atmospheres, the metal is evaporated, forming a film on the wafer surface placed above the boat.

2.2.2 Patterning Process

As mentioned in the previous section, the photoresist material is first spun onto the wafer surface at a constant speed for 30 seconds. The wafer is then "soft-baked" for 50 seconds on a hot plate at 110°C to remove most of the solvent present in the resist. The mask and wafer are then placed in the mask aligner and aligned to each other. Ultraviolet light is then shone on to the pair, chemically altering the exposed resist. The wafer is then developed using a mild base, and rinsed with de-ionized water.

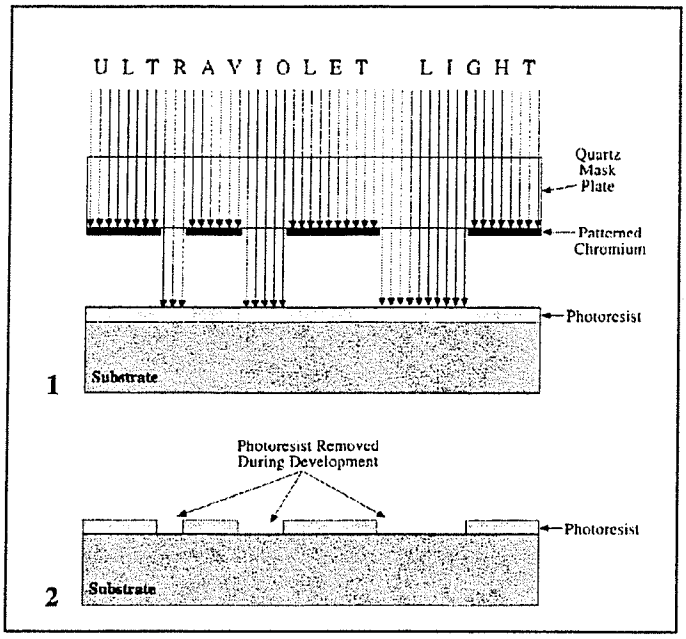

Figure 2.6: *Basic photolithographic process employed with positive resist [5].*

There are two types of photoresist; positive and negative. Positive photoresist allows the regions exposed to UV light to wash away with the base, as shown in Figure 2.6, leaving a positive impression of the mask. Whereas the negative photoresist allows the base to wash away the unexposed regions of the wafer, thus leaving a negative image of the mask. Positive resist is more widely used today since negative resist has a limited resolution of about 2 μm.

2.2.3 Removal Processes

Removal processes by chemical or mechanical means, also known as etching, can be done to the surface or bulk of the wafer. Etchants are classified according to their nature and behaviour. In terms of nature, etchants can be labelled as wet or dry etchants. Furthermore, their behaviour is crucial for the type of geometry desired. Isotropic etchants etch all directions at a uniform rate resulting in rounded features. Anisotropic etchants, also known as "orientation dependent", etch much faster in one direction than in

another. Figure 2.7 illustrates the isotropic and anisotropic etchant profiles for wet etchants.

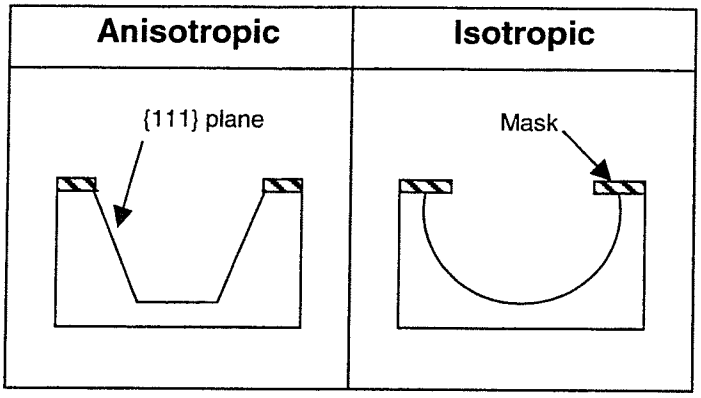

Figure 2.7: *Isotropic and anisotropic wet etchant profiles [6].*

Wet and dry etchants are selected on the basis of specific characteristics such as selectivity to etch masks, availability to etch-stop methods, etch rate, degree of surface roughness created, safety, disposal difficulty, circuit compatibility, cost and many more [5]. Wet etchants in aqueous solution offer the advantage of low-cost batch fabrication; usually 20–25 wafers can be etched simultaneously. Dry etching, on the other hand involves the use of reactant gases in low-pressure plasma [6]. Common wet etchants such as potassium hydroxide (KOH), ethylene diamine pyrochatechol (EDP), and tetra methyl–ammonium hydroxide (TMAH) result in anisotropic etchant profiles, whereas the dry vapour-phase etchant, XeF_2, is an isotropic etchant of silicon.

2.3 Mathematical Model of Corrugated Membranes

The analytical expression for the spring constant k of a sinusoidally corrugated membrane is given by equation (2.13) [8]. The sinusoidal corrugations are patterned and etched onto the surface of the membrane to increase its flexibility.

$$k = \frac{A_p \pi E t^3}{R^2} + \frac{B_p E t z^2}{R^2} \tag{2.13}$$

where the constants A_p and B_p , and the quality factor q are given by:

$$A_p = \frac{2(q+2)(q+1)}{3\left(1-\left(\frac{\nu}{q}\right)^2\right)} \tag{2.14}$$

$$B_p = \frac{32}{(q^2-9)}\left(\frac{1}{6} - \frac{3-\nu}{(q-\nu)(q+3)}\right) \tag{2.15}$$

$$q = \sqrt{\frac{S}{L}\left(1+\frac{3}{2}\left(\frac{H}{t}\right)^2\right)} \tag{2.16}$$

and E is Young's modulus, R is the membrane's radius, t is the membrane's thickness, z is the vertical deflection, ν is Possion's ratio, H is the corrugation height, S the corrugation arc length, and L the corrugation period. The corrugation parameters S, L, H, and t are illustrated in Figure 2.8.

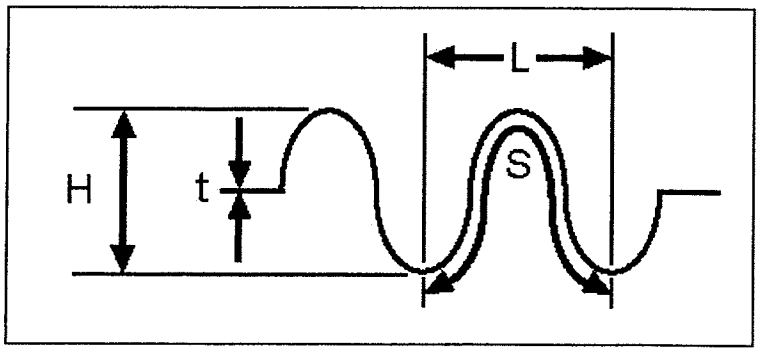

Figure 2.8: *Corrugation parameters [7].*

The membrane's quality factor depends on the corrugation height, arc length and on the membrane's thickness. Results obtained by Chrusch illustrate that to obtain large deflections; a large corrugation quality factor is desired [7]. A comparison between a flat 10 mm diameter copper membrane to a corrugated membrane of diameter 10 mm is illustrated in Figure 2.9. The corrugated membrane's parameters include a corrugation height of 5 μm, and a pitch of 112 μm. The corrugated membrane proves to be more flexible, and requires approximately 10% less of the force needed for a total deflection of 300 μm compared to the flat membrane.

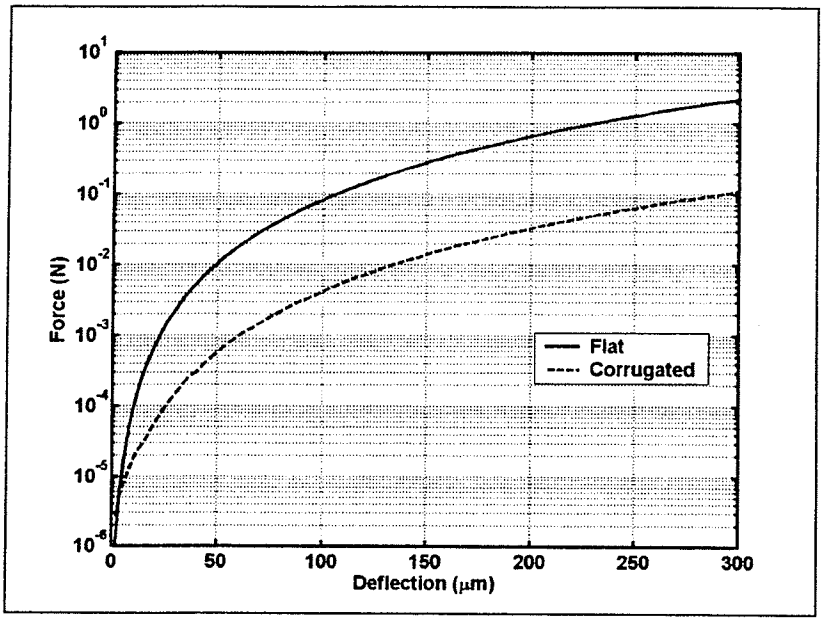

Figure 2.9: *The force required to actuate a flat and corrugated membrane [7].*

The membrane is placed in the jig illustrated below for electrostatic actuation, where z is the measure of vertical deflection experienced by the corrugated membrane.

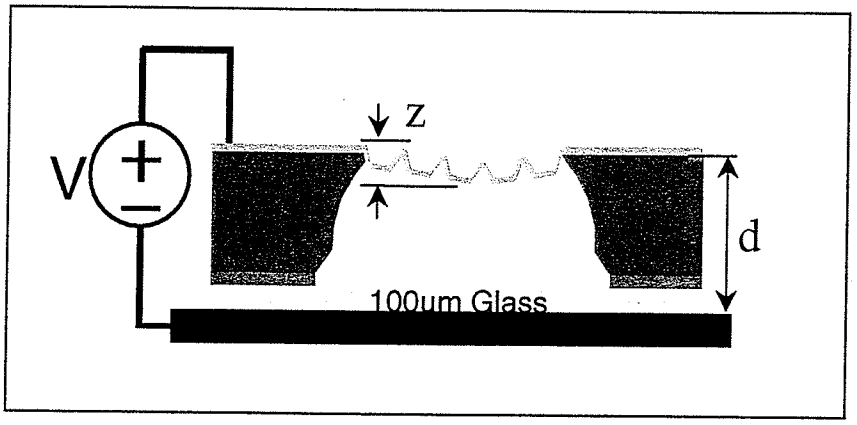

Figure 2.10: *Electrostatic actuation set-up [7].*

A driving voltage is applied between the corrugated membrane and lower driving electrode for electrostatic actuation. To prevent any electrical shorting, a 100 μm glass sheet is placed between the driving electrode and corrugated membrane as an insulation layer. The actuation voltage for a circular membrane can be derived from a parallel plate capacitor's energy equation and is given by equation 2.17.

$$V = \sqrt{\frac{2kz(d-z)^2}{\varepsilon\pi R^2}} \tag{2.17}$$

where k is the spring constant, z is the membrane's vertical deflection from its initial state, d is the distance between the wafer surface and the driving electrode, and R is the membrane's radius. This equation is valid for small deflections; however, with larger deflections, the membrane's curvature increases, and this simple parallel plate capacitor derivation will no longer apply [7].

The voltage required to move the corrugated membrane can be lowered by reducing the distance between the driving electrode and membrane, as shown in Figure 2.11 (a). The corrugated membrane is turned over, and 200 μm thick sheets of glass are used to raise the membrane above the 100 μm insulation glass layer. From equation (2.17), reducing z from approximately 400 μm to 200 μm, will decrease the voltage

applied. This voltage decrease is observed in the simulation results shown in Figure 2.11 (b). For instance, to deflect a corrugated membrane by 150 μm, 1120 volts are required for the 400 μm spacing, but only 400 volts are needed for the 200 μm spacing.

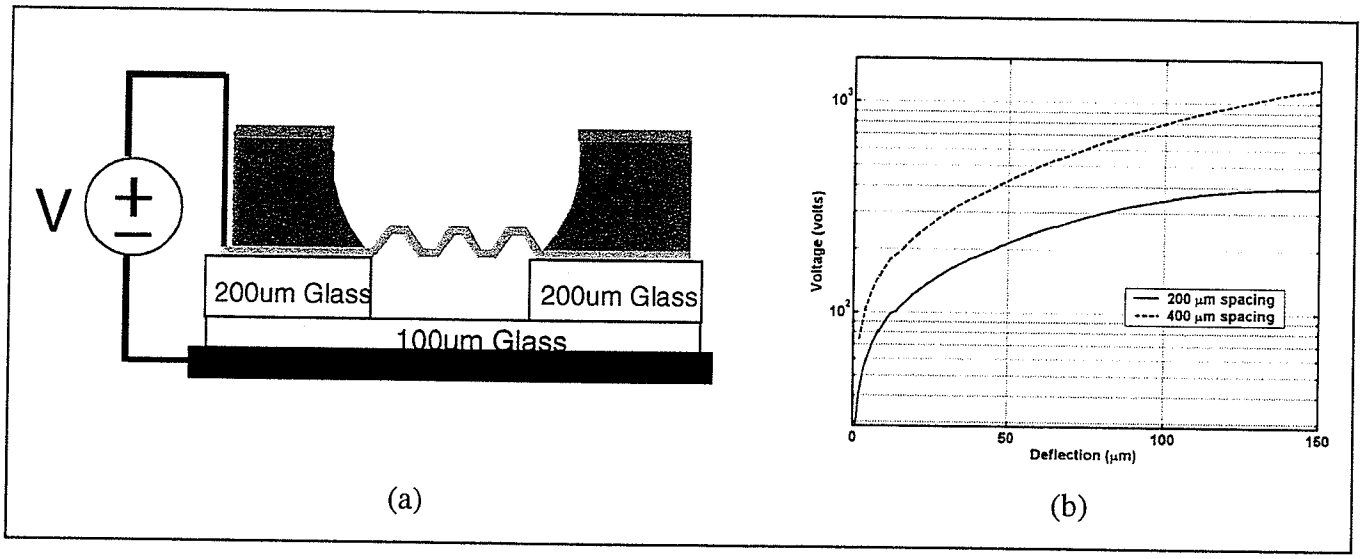

Figure 2.11: *(a) 200 μm air-gap electrostatic actuation set-up, (b) comparison of the voltage required for the 200 μm and 400 μm spacing.*

Chapter 3

Antenna Models and Simulation Results

This chapter introduces the three models initially considered for an adjustable air-gap MPA. The model with maximum frequency-shift was then designed at different frequencies and simulated to observe the antenna behaviour with varying air-gap thickness. The model geometry and dimensions are presented along with the simulated results obtained. Variations of the chosen model were also investigated at different air-gap heights.

3.1 The Initial Models Considered

This section describes the three models considered to obtain a maximum allowable range of frequency shift, and presents the simulated results obtained. The three models proposed for the frequency-tunable MPA are illustrated in Figure 3.1. Model 1 consists of a patch element on a 100 μm thick glass suspended over an air-gap layer and ground plane. In Figure 3.1 (b), Model 2 is the reciprocal of Model 1, in which the air-gap and the 100 μm thick glass positions are interchanged. Finally Model 3 consists of two glass sheets 100 μm thick separated by an air-gap. In all three models, the air-gap thickness varies from 0 to 1 mm in thickness.

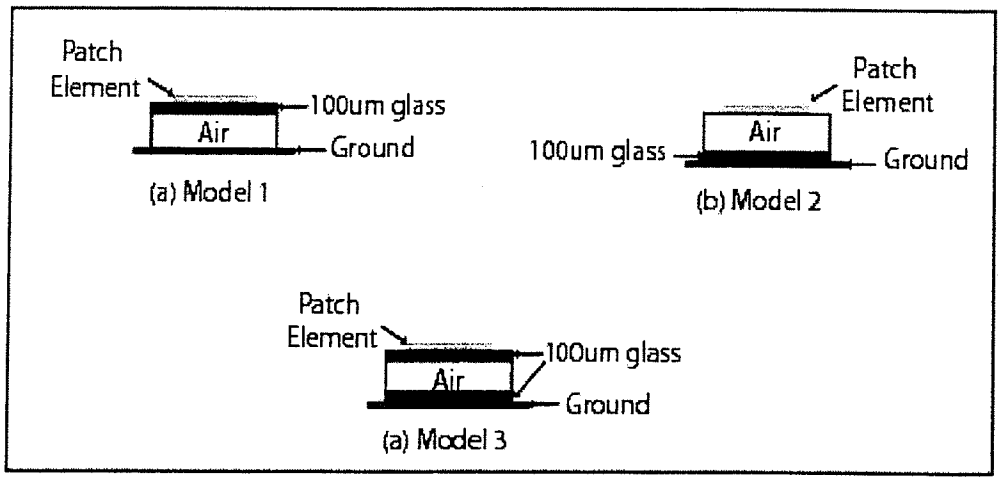

Figure 3.1: *Three models of an adjustable air-gap microstrip patch antenna.*

The AF 45 (Alkali-Free Thin Glass) 100 μm thick glass sheet's properties include a permittivity of 6.2 and a loss tangent of 0.0009.

The three models proposed for the frequency-tunable MPA were modelled in Ensemble 8.0 for comparison, where the software assumes an infinite ground plane and glass layer. The simulated results for the three models at a resonant frequency of 8.8 GHz with increasing air-gap thickness are illustrated in Figure 3.2.

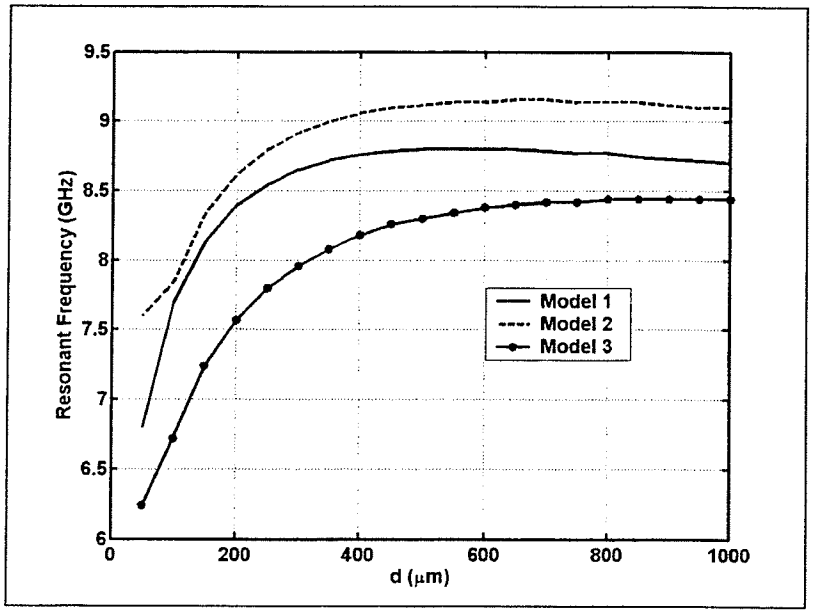

Figure 3.2: *Simulated results for the three models with varying air-gap height.*

Comparing the plots in Figure 3.2, Model 1 provides the steepest slope, i.e. a larger frequency shift, compared to that of Models 2 and 3 for the first few hundred microns of air. Therefore, Model 1 is the optimum design and was chosen for the bulk and micromachined antenna designs.

3.2 Model 1 at Several Resonant Frequencies

Model 1 behaviour at several resonant frequencies is then evaluated. A 5 GHz, 8.8 GHz and 18.9 GHz MPA were modeled and simulated in Ensemble with increasing air-gap height. The results obtained are illustrated in Figure 3.3. As the thickness of the air layer is increased, the effective dielectric constant reduces as shown in Figure 3.3 (a). As a result, the resonant frequency increases resulting in approximately a 5% to 12% range of shift in operating frequency for the three frequency curves shown in Figure 3.3 (b) for the first few hundred microns of deflection.

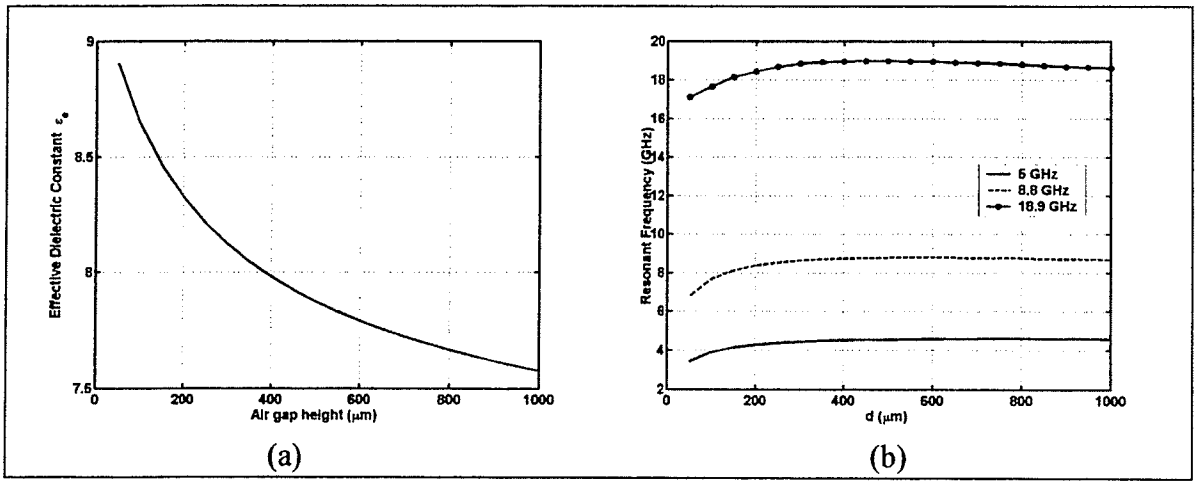

Figure 3.3: *(a) The decreasing of ε_e with increasing air-gap height, and (b) the simulated results for the 5 GHz, 8.8 GHz and 18.9 GHz models at different air-gap heights.*

The maximum amount of frequency shift occurs within the first few hundred microns. However beyond approximately 300 μm of air, the resonant frequency plateaus, and past 600 μm of air-gap thickness, the resonant frequency gradually drops. The behaviour of these curves may be explained by several phenomena including: fringing fields and the inverse relationship between the resonant frequency and the effective dielectric constant as deduced from equation (2.3).

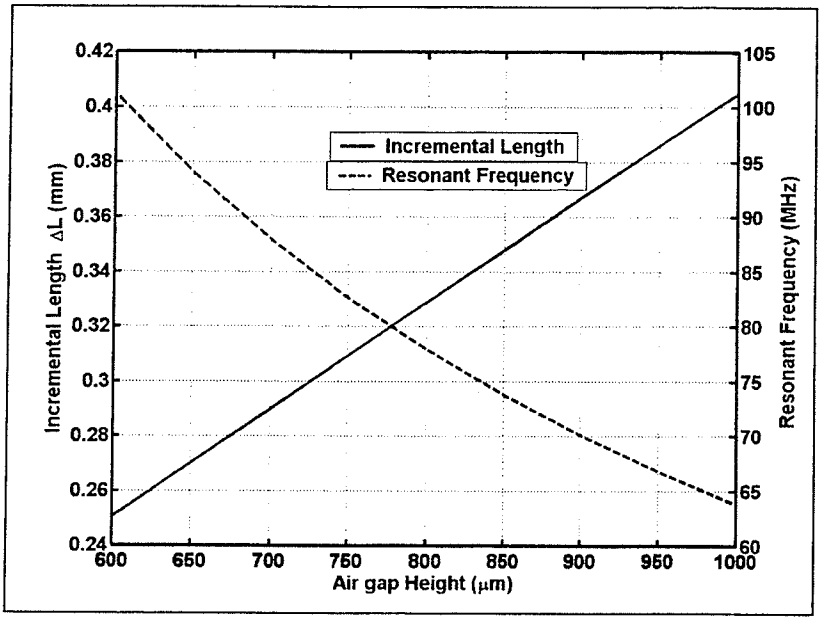

Figure 3.4: *Behavior of the patch's incremental length with increasing air-gap thickness.*

These effects are explained by plotting the frequency response and incremental fringing length of an 8.8 GHz antenna using the empirical formulae presented in Section 2.1.2. At small thickness of the air layer (between 0 μm to 200 μm), the fringing effect is minimal, and the curve is mostly traced out by the inverse relationship between the dielectric constant and the resonant frequency. With increasing thickness of the air layer, the dielectric constant is decreasing in value, resulting in an increase in the resonant frequency, as shown earlier in Figure 3.3 (a). However, when the thickness of the air

layer is large (past 600 μm), the fringing effect is more pronounced and begins to manipulate the results of the graph. This can be seen in Figure 3.4, which reveals a change in resonant frequency due to fringing assuming a constant ε_e. Between 600 μm – 1000 μm, the resonant frequency decreases by approximately 40 MHz. This may explain the slight decrease in the curve past the air layer height of 600 μm in Figure 3.3 (b).

3.3 Model 1 with Varied Glass Thickness

The effect of the glass sheet thickness is explored in this section. The original 20 GHz antenna with a 100 μm thick glass sheet is compared to a 20 GHz antenna with a 200 μm and 500 μm thick glass sheet. The plot comparing the simulated results obtained is shown in Figure 3.5.

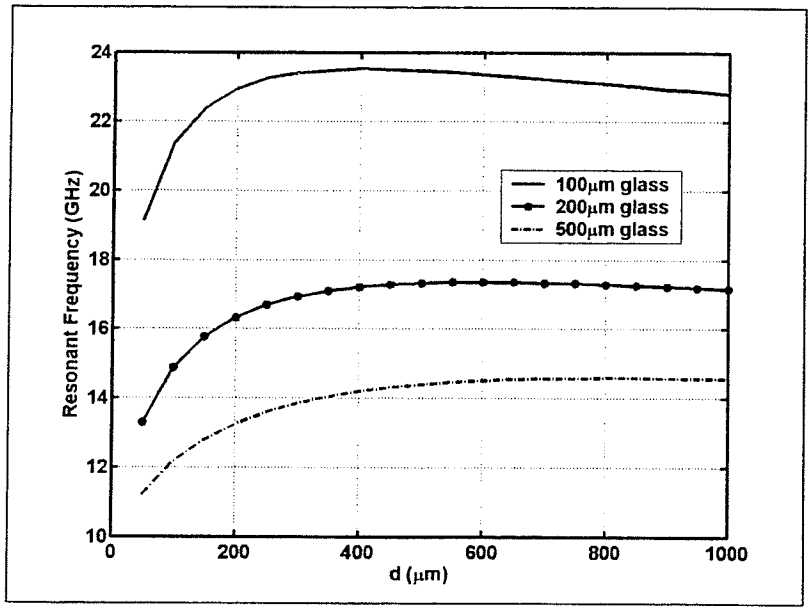

Figure 3.5: *Comparison of the simulated results for the different thickness glass layer models with varying air-gap.*

Model 1 with a 100 μm thick glass provides the steepest slope within the first few hundred microns. The curves also illustrate that with increasing glass thickness, the dielectric constant is larger, and as expected the resonant frequency is lower.

Chapter 4

Bulk Model Fabrication and Results

The bulk model's fabrication procedure and design are presented in this chapter. There are two antennas designed and presented, an 8.8 GHz and 18.9 GHz antenna, to confirm the behaviour of the simulation results obtained and presented in Chapter 3. The antenna dimensions and software considerations are discussed in detail. Also, the measured return loss curves and radiation patterns are compared to the simulated results. Finally, possible sources of errors are then discussed to explain the discrepancies present between the measured and simulated results.

4.1 Bulk Model Fabrication

The design and fabrication of the bulk antenna model requires several of steps including: the fabrication and design of the patch antenna, and the structural design of the jig, and the connection of the antenna to a Sub-Miniature version A (SMA) high-frequency connector.

4.1.1 MPA Design and Fabrication

The MPAs are designed and optimized using Ensemble software 8.0 to operate at a resonant frequency of 8.8 GHz, and 18.9 GHz. The empirical formulae presented in Chapter 2 are used to calculate the patch, quarter-wave transformer and 50 Ω feed-line dimensions. The input impedance of the patch was calculated as approximately 250 Ω by

Ensemble, resulting in a 100 Ω line for the quarter-wave transformer line. The antenna dimensions are presented in Table 4.1.

Table 4.1: 8.8 GHz and 18.9 GHz antenna dimensions.

	Patch Antenna Dimensions		Quarter-wave t-line Dimensions		50 Ω t-line Dimensions	
	Length *(mm)*	Width *(mm)*	Length *(mm)*	Width *(mm)*	Length *(mm)*	Width *(mm)*
8.8 GHz Antenna	14.35	17.23	6.94	1.487	5	4.57
18.9 GHz Antenna	5.82	7	4.25	1.2803	3	4.57

The conventional method of using a razor to cut out the patch antenna is difficult and inaccurate at such small dimensions. Therefore, the copper patch antennas are thermally evaporated onto the 2 inch square glass sheet. A shadow mask is first designed using Ensemble, then milled onto some Printed Circuit Board (PCB) material using a milling bit with a tip of resolution 0.0002 inches.

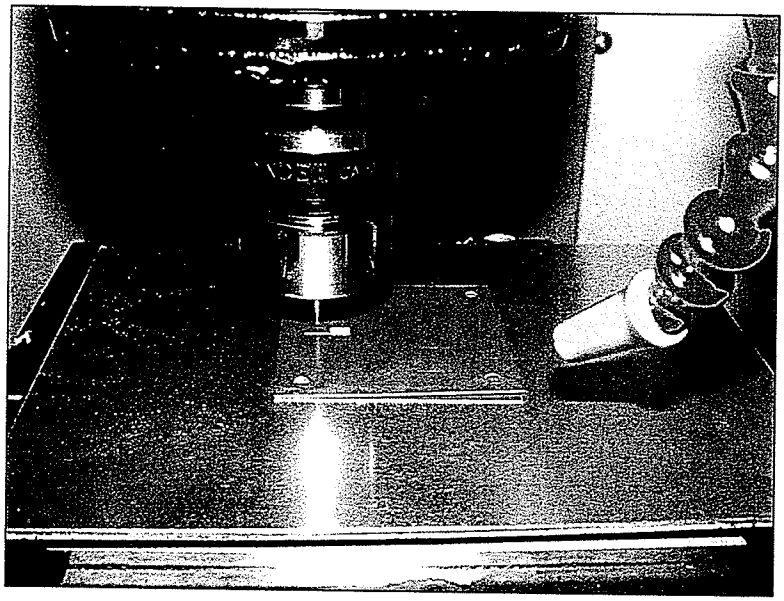

Figure 4.1: *PCB mask and milling machine tip.*

This mask and AF-45 glass sheet are then cleaned and prepped for the evaporation chamber, where the copper is evaporated through the mask and onto the AF-45 glass sheet. First, 21 nm of chrome is evaporated onto the glass sheet to aid in the copper's adhesion to the glass sheet. Next, 1.647 μm of copper is evaporated on top. Attention must be paid to the thickness of the copper layer to avoid any losses induced due to skin effect, in which the wave travelling through the conductor exponentially decreases. The skin depth or penetration depth in this case is calculated using Equation (4.1),

$$\delta = \frac{1}{\sqrt{\pi f \mu \sigma}} \tag{4.1}$$

where the conductivity of copper (σ) is 5.8×10^7 mhos/m. The skin depths for the two frequencies of interest are revealed in Table 4.2.

Table 4.2: *The skin depth in copper at 8.8 GHz and 18.9 GHz.*

Frequency (GHz)	8.8 GHz	18.9 GHz
Skin depth (μm)	0.705	0.481

The standard recommended thickness is usually around three times the skin depth. Ensemble software assumes a default thickness of 17.5 μm of copper (1/2 ounce) for traces [9].

4.1.2 Bulk Model Structure Design

The bulk model consists of several components including: ground plane, the MPA evaporated on glass, an SMA connector, and the three micrometers. The ground plane consists of three aluminium slabs labelled in Figure 4.2; the base ground plane (1) connected to the moving ground block (2) with a screw, and the outer frame ground plane (3) connected to the moving ground block with two screws sitting in a shaft.

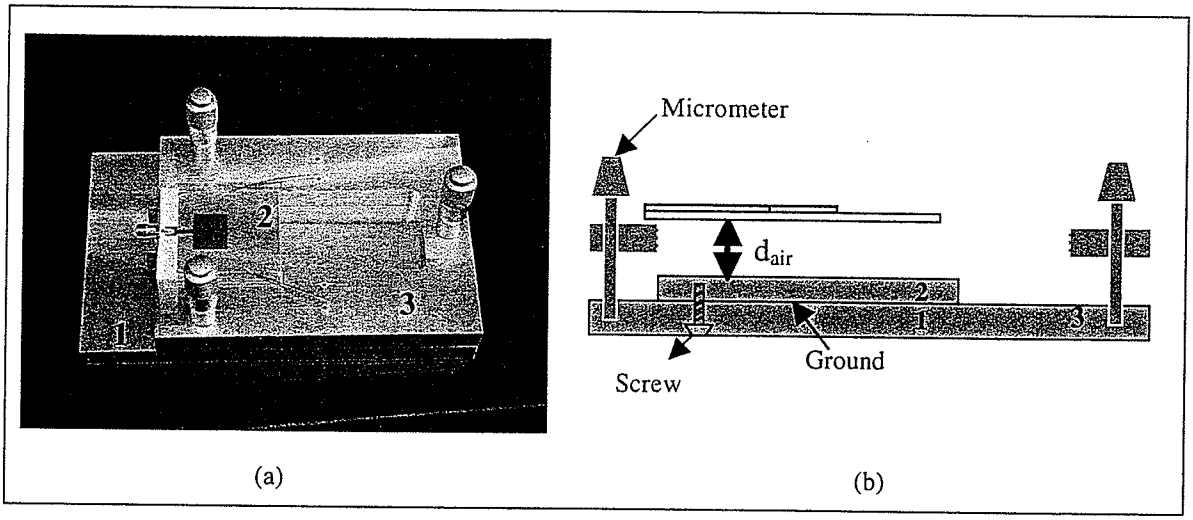

Figure 4.2: (a) Top view and (b) side view of the bulk-machined model.

The MPA evaporated on a 100 μm glass sits on top of the moving ground held in place using two metal pins. The three micrometers are placed in a tripod configuration, and are used to move the moving ground block 1 mm in 0.05 increments. The dimensions of the bulk structure with all of its components are illustrated in the Figure 4.3.

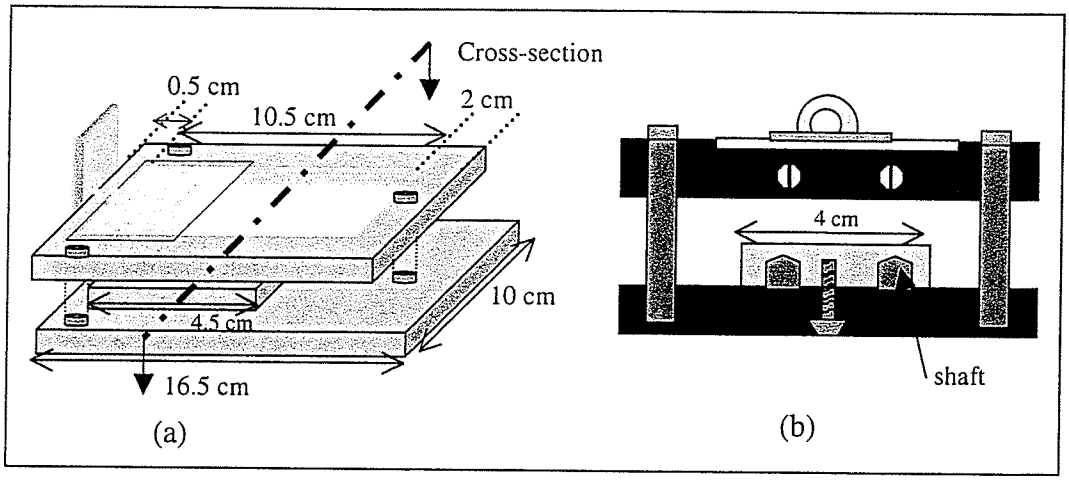

Figure 4.3: Dimensions of the bulk-machined model structure.

4.1.3 SMA Connection

The typical transition from a coaxial line to the MPA is to extend the inner conductor of an SMA connector and solder it to the 50 Ω feed line. In this case however, the high-frequency SMA probe could not be soldered on to the microstrip patch antenna because the heat required to melt the solder disperses quickly through the thin layer of copper. EPO-TEK H20E, a two component silver filled Epoxy designed specifically for chip bonding in microelectronic and optoelectronic applications, is used instead to bond the SMA probe to the antenna. The cure schedule dictates an 80°C bake for 90 minutes for the Epoxy to harden.

4.2 Bulk Model Results

The measured results obtained for the 8.8 GHz and 18.9 GHz antennas are presented in this section and compared to the simulated results obtained from Ansoft's Ensemble software. Measured results include the return loss plots (S_{11}) obtained from the Vector Network Analyzer (VNA), and radiation patterns measured in the anechoic chamber.

4.2.1 8.8 GHz Antenna Results

The 8.8 GHz antenna with dimensions mentioned in the previous section was fabricated and placed in the bulk-machined set-up model and its reflection coefficient, S_{11}, was then measured using the VNA. A comparison of the measured and simulated is shown in Figure 4.4.

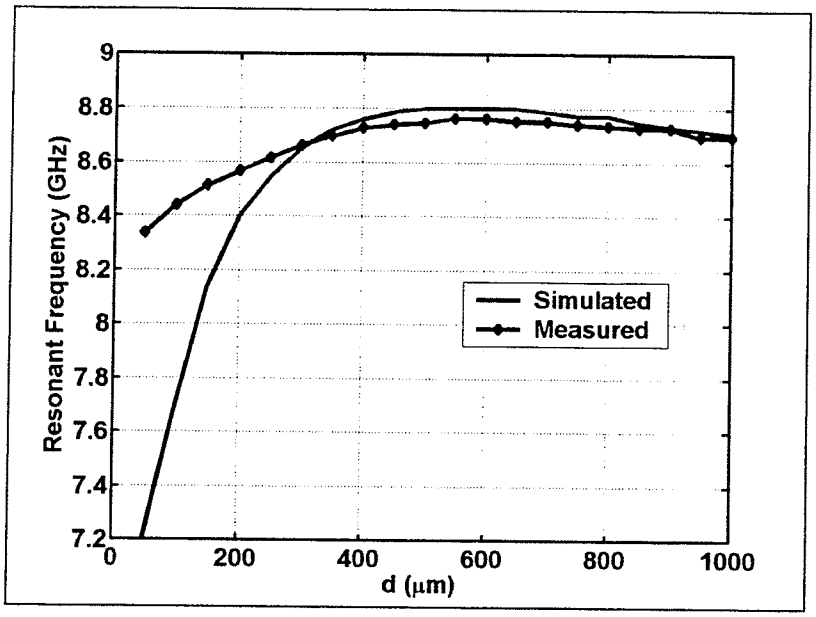

Figure 4.4: *A comparison of the 8.8 GHz antenna's simulated and measured resonant frequencies for increasing air-gap height.*

The simulated results provide a frequency shift of 667 MHz with a steeper slope, whereas the measured results provide a frequency shift of 400 MHz. The potential causes of the discrepancies present between the simulated and measured are described in Section 4.3.

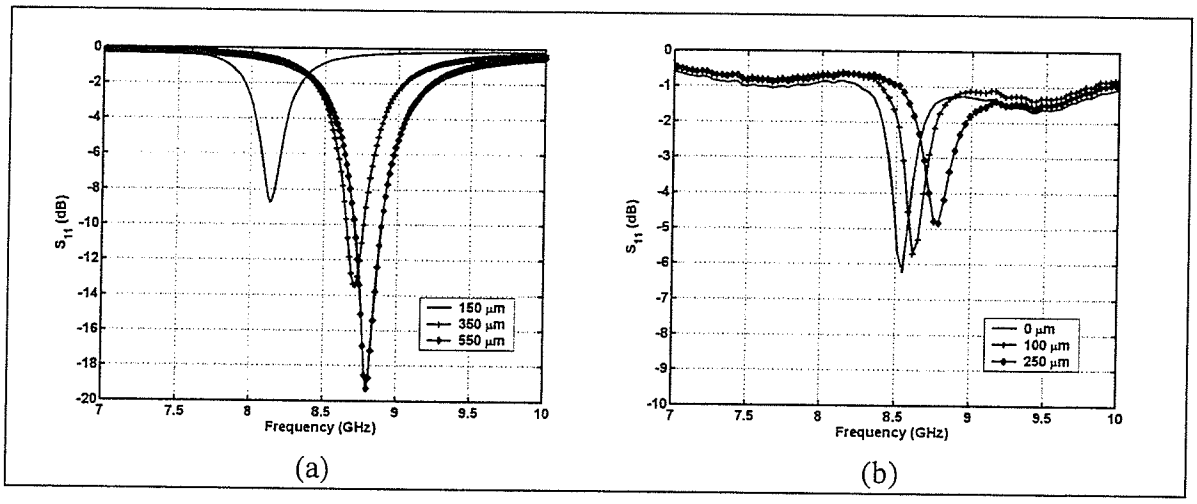

Figure 4.5: *A comparison of the S_{11} plots for different air-gap heights obtained from (a) Ensemble Simulations, and (b) measured on the VNA.*

The antenna's radiation patterns were also measured and compared to the simulated results. To measure the radiation patterns the micrometers are removed to minimize reflections, and copper shims are inserted to raise the ground frame (c). These shims were ordered at different thickness in inches and are cut and placed only beneath the aluminium slab, so that the ground plane connection remains the same. The antenna is placed in University of Manitoba's anechoic chamber for radiation patterns, as shown in Figure 4.6.

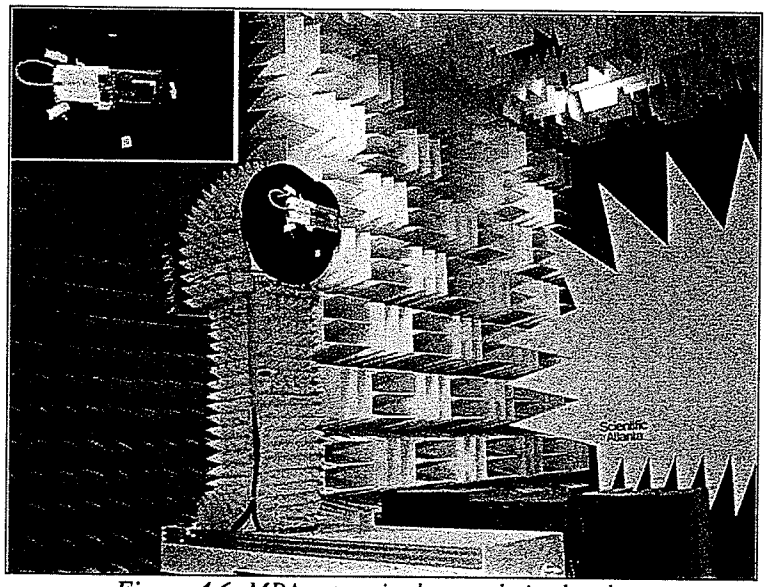

Figure 4.6: *MPA set-up in the anechoic chamber.*

The co-polarization components of the E and H field, and the E co-polarization and cross-polarization components are measured and compared to the simulated results in Figures 4.7 and 4.8 sequentially. Simulated and measured Smith charts are included in the Appendix for reference.

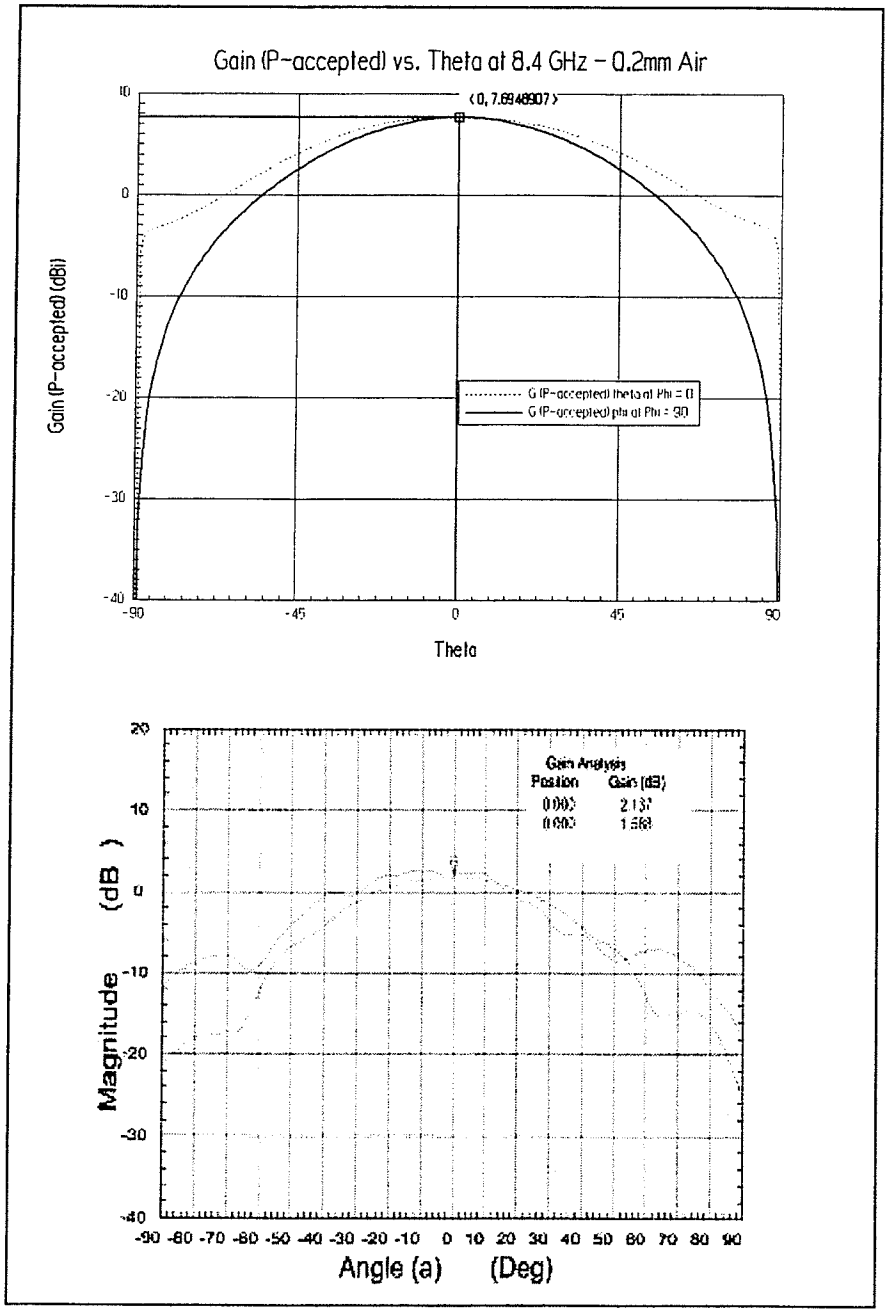

Figure 4.7: *Comparison of the 8.8 GHz antenna simulated and measured E and H co-polarization radiation patterns.*

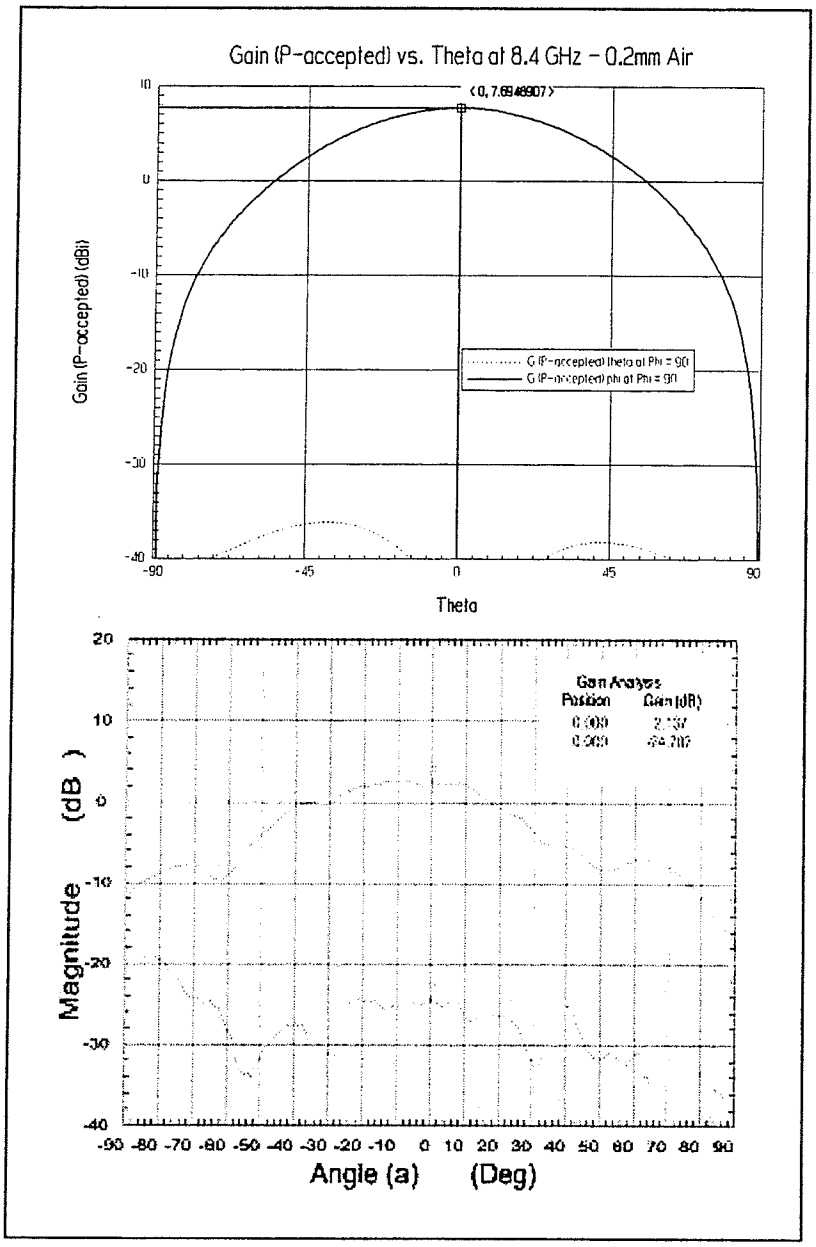

Figure 4.8: *Comparison of the 8.8 GHz antenna simulated and measured E co-polarization and cross-polarization components.*

The measured radiation patterns are also very close in behavior with a gain of 2.137 dB for the E field, and 1.568 dB for the H field. The measured gains are observed to be lower than the simulated gain of 7.694 dB. The E field's measured cross polarization component remains below the -20 dB level.

4.2.2 18.9 GHz Antenna Results

The 8.8 GHz antenna is then removed and replaced with the 18.9 GHz antenna. Initially, the model with a 50 Ω feedline matched to the patch with a quarter wave transformer was resonating and impeding the performance of the antenna, as shown in the S_{11} plot in Figure 4.9 at a frequency of 24.236 GHz. This 50 Ω line's dimensions were very close to the patch element size.

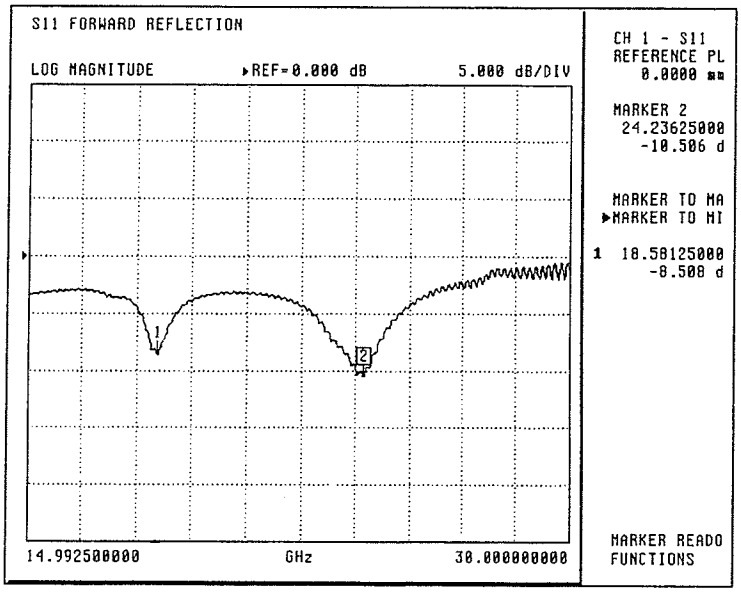

Figure 4.9: *S_{11} plot measured for the 18.9 GHz antenna with the 50 Ω feedline.*

Trimming off the 50 Ω feed line improved the antenna's performance, and the measured frequency shift is compared to the simulated frequency shift is Figure 4.10. The simulated results provide a frequency shift of 1.066 GHz, whereas the measured results provide a frequency shift of approximately 400 MHz. The S_{11} plots are also compared in Figure 4.11 for different air-gap heights.

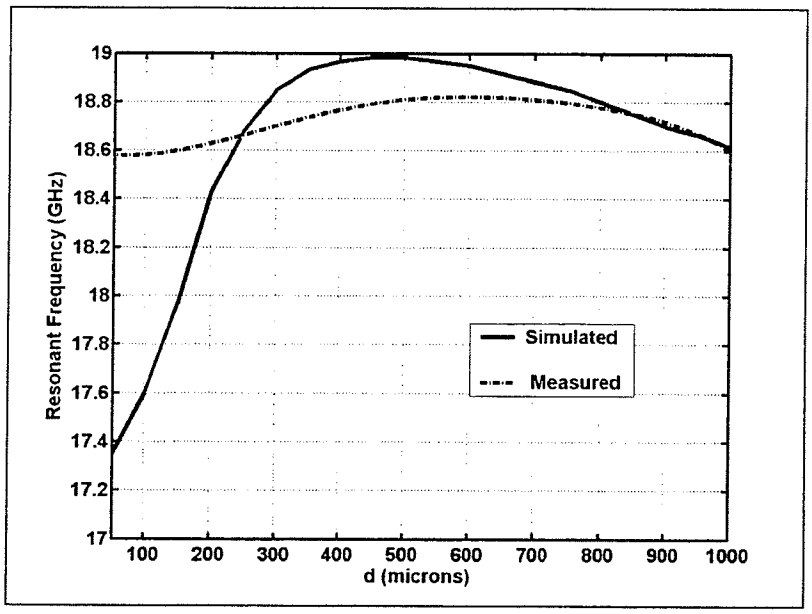

Figure 4.10: *Comparison of the 18.9 GHz antenna's Ensemble simulated and VNA measured resonant frequencies for varying air- gap heights.*

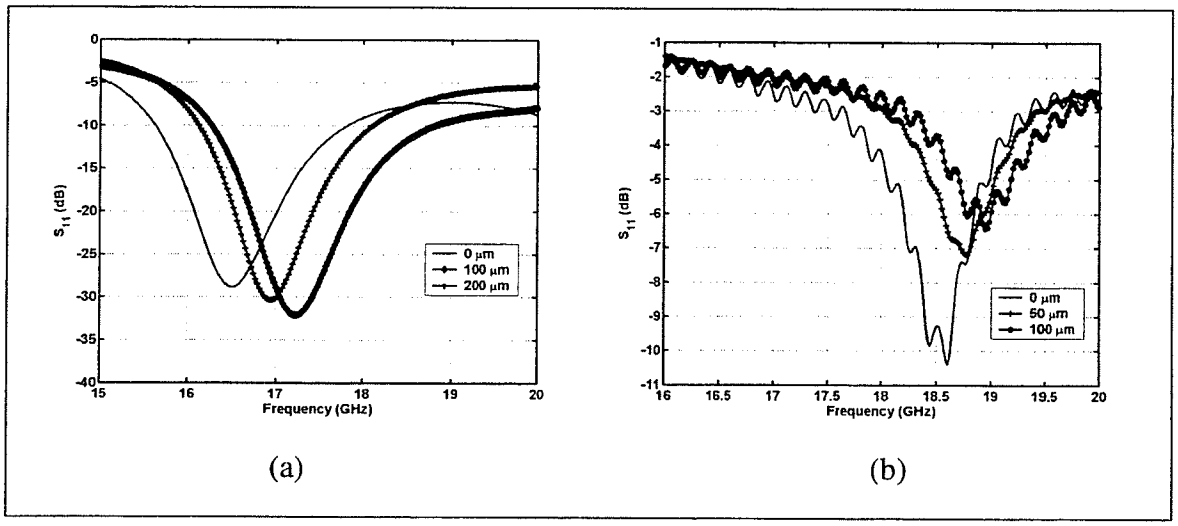

Figure 4.11: *A comparison of the S_{11} plots for different air-gap heights obtained from: (a) Ensemble Simulations, and (b) measured on the VNA.*

Similar to the procedure followed for the 8.8 GHz antenna, the 18.9 GHz antenna's radiation patterns were also measured and compared to the simulated patterns. The presence of the air-gap does not affect the antenna's radiation patterns. The measured radiation patterns are illustrated in Figures 4.12 and 4.13.

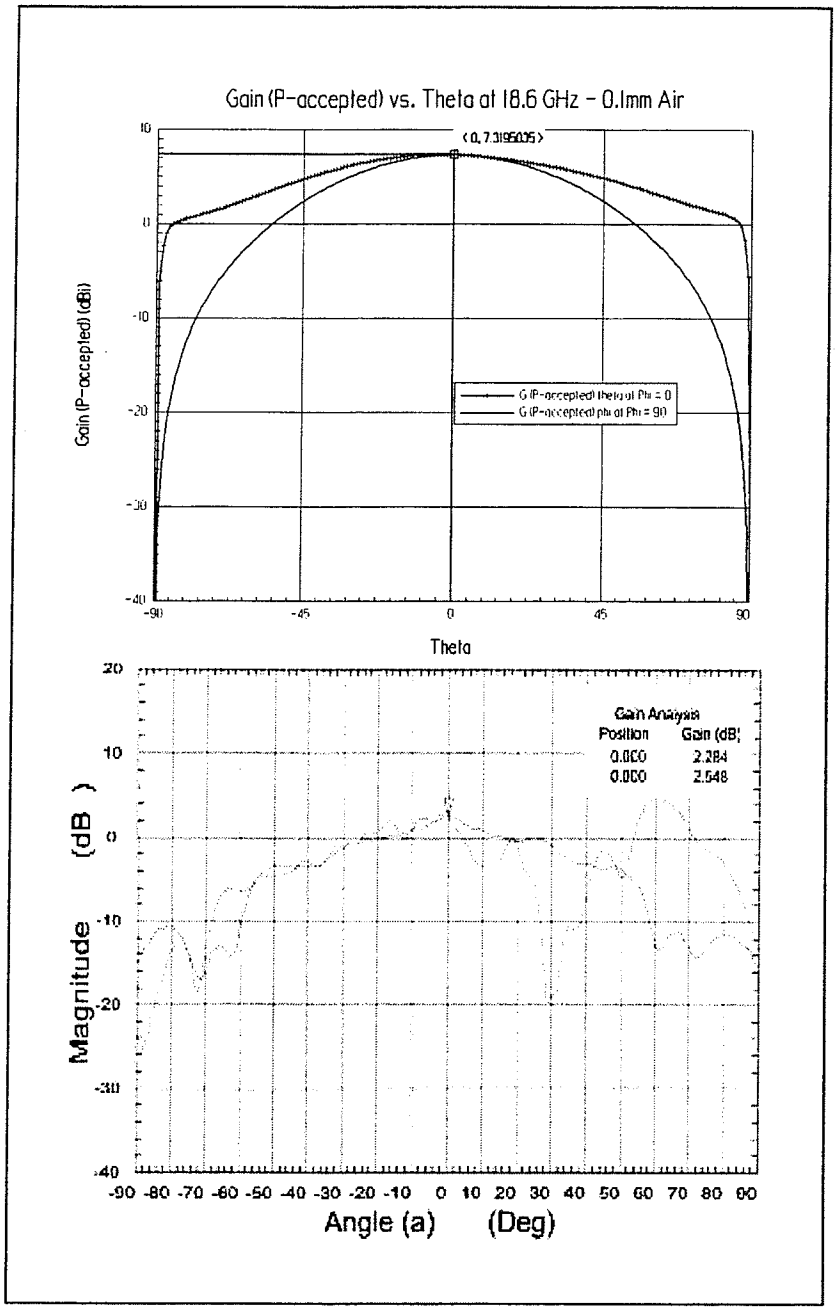

Figure 4.12: *Comparison of the 18.9 GHz antenna simulated and measured E and H co-polarization radiation patterns.*

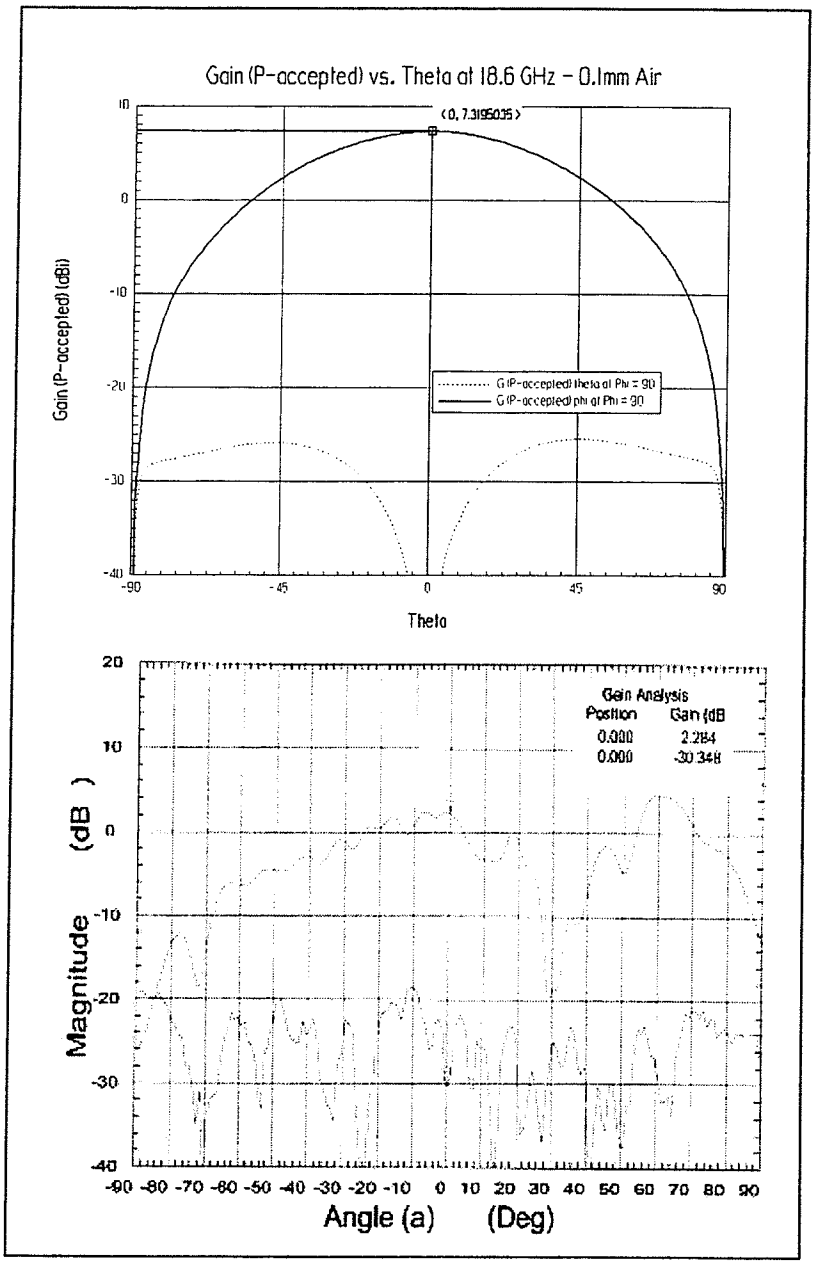

Figure 4.13: *Comparison of the 18.9 GHz antenna simulated and measured E co-polarization and cross-polarization components*

Table 4.3: *Simulated and measured frequency shift results for the 8.8 GHz and 18.9 GHz antennas at air-gap heights varying from150 μm to 500 μm.*

	Simulated Results Frequency Shift (MHz)	**Measured Results Frequency Shift (MHz)**
8.8 GHz Antenna	667	400
18.9 GHz Antenna	1066.7	400

Table 4.3 shows that the bulk-machined models for the 8.8 GHz and 18.9 GHz antennas tested were found to experience a considerable shift in resonant frequency.

4.3 Sources of Error

There are several possible sources of error present in the model structure design and fabrication that justify the slight variations between the simulated and measured results. Factors such as Epoxy loss, the inaccuracy of the micrometers and the finite-sized ground plane affect the performance of the antenna.

4.3.1 Losses

There are two losses present in the model that are of concern including the Epoxy connection loss and the thickness of the copper evaporated (i.e. skin depth).

In the bulk-machined model, the Epoxy paste is placed on the tip of the probe and on the sides of the SMA connector for an improved connection to the ground plane, since soldering could not be used as mentioned earlier in Section 4.1.3. The inherent discontinuity of the currents in the vicinity of the transition from connector to feed line is

a source of radiation and surface wave losses. To evaluate the loss of Epoxy, two 50 Ω transmission lines at 10 GHz are designed.

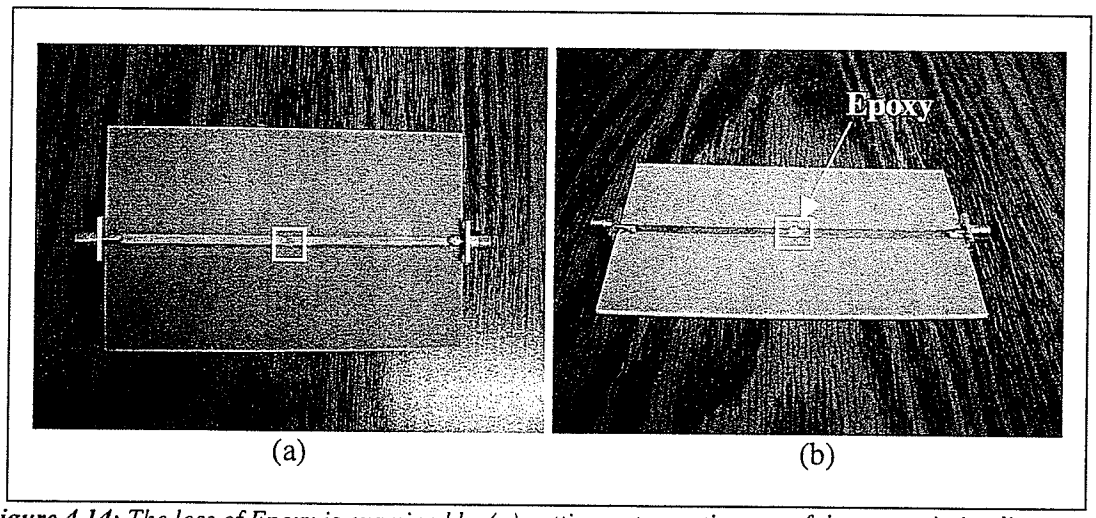

Figure 4.14: *The loss of Epoxy is examined by (a) cutting out a section out of the transmission line, and (b) placing some Epoxy as a connection.*

The first transmission line is treated as the reference line and its reflected and transmitted parameters (S_{11} and S_{21}) are measured. A 1 cm square slot is cut out of the second transmission line, and Epoxy is placed at the centre for a connection and baked, as illustrated in Figure 4.14. Its S_{11} and S_{21} parameters were then measured. Figure 4.15 presents a comparison of the two transmission lines' behaviour in terms of S_{11} and S_{21} plots.

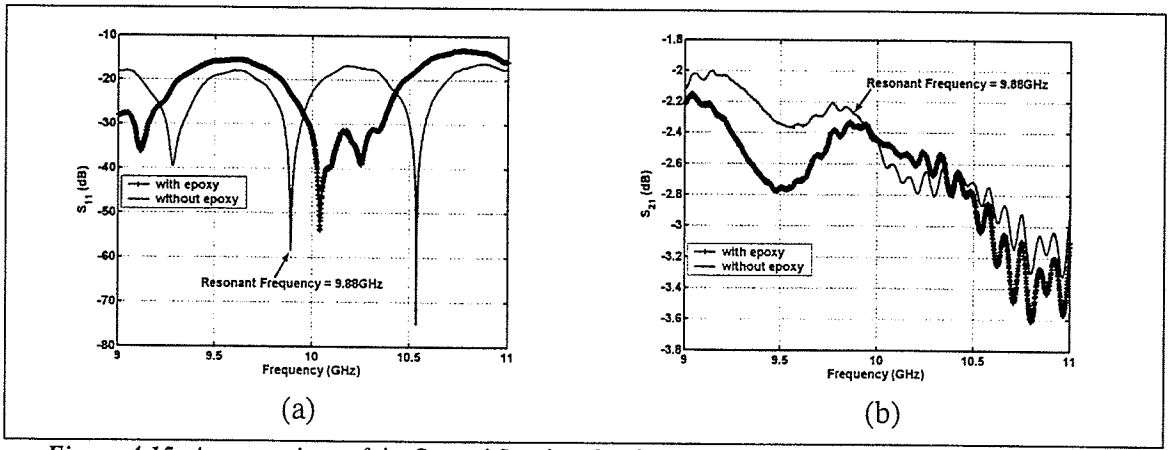

Figure 4.15: *A comparison of the S_{11} and S_{21} plots for the transmission lines with and without Epoxy.*

From Figure 4.15(a), the presence of Epoxy results in an increase in reflection loss by approximately 30 dB. Moreover, the Epoxy increased the loss in the transmission line to –2.4 dB. Therefore, the use of Epoxy as a connection is found to slightly degrade the antenna's performance.

In terms of skin depth losses, two 50 Ω transmission lines resonating at 10 GHz with different copper layer thickness evaporated on Corning™ 1737 glass sheets are compared. The first transmission line has a copper thickness of 1.25 μm, and the second has triple the copper thickness of 2.8 μm. As mentioned earlier, Ensemble software assumes a default thickness of 17.5 μm of copper for traces, which is 5 – 18 times more than the transmission lines.

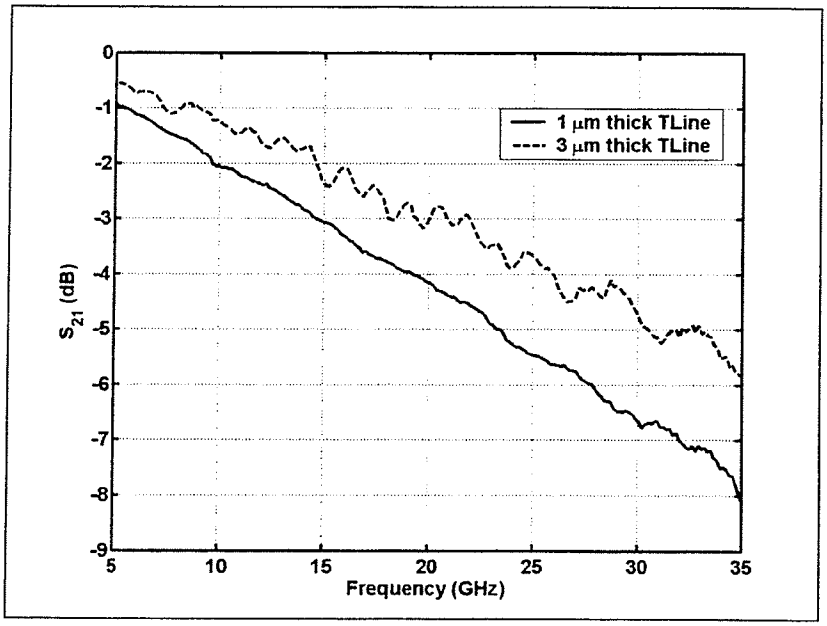

Figure 4.16: *A comparison of the S_{21} plots for the transmission lines of 1.25 μm and 2.8 μm copper thickness.*

The S_{21} plots shown in Figure 4.16 illustrate a substantial amount of improvement in the insertion loss by increasing the trace layer's thickness. Therefore, increasing the

copper layer thickness to 2.8 μm (approximately 4 times the skin depth at 10 GHz) reduces the amount of skin effect losses by almost 2 dB.

4.3.2 Non-parallel Geometry

The ground plane beneath the patch is not 100% parallel to the patch. This can be due to an offset in the micrometers and the unevenness of the metal shims used in radiation pattern measurements. As a result, this leads to uneven fields in the different areas between the patch and the ground plane, inducing several modes and resulting in impedance mismatches and loss in energy. To study this phenomenon, a probe-fed 2 GHz MPA was designed sitting over an air-gap shown in Figure 4.17. The antenna is tilted in several directions and the matching was observed.

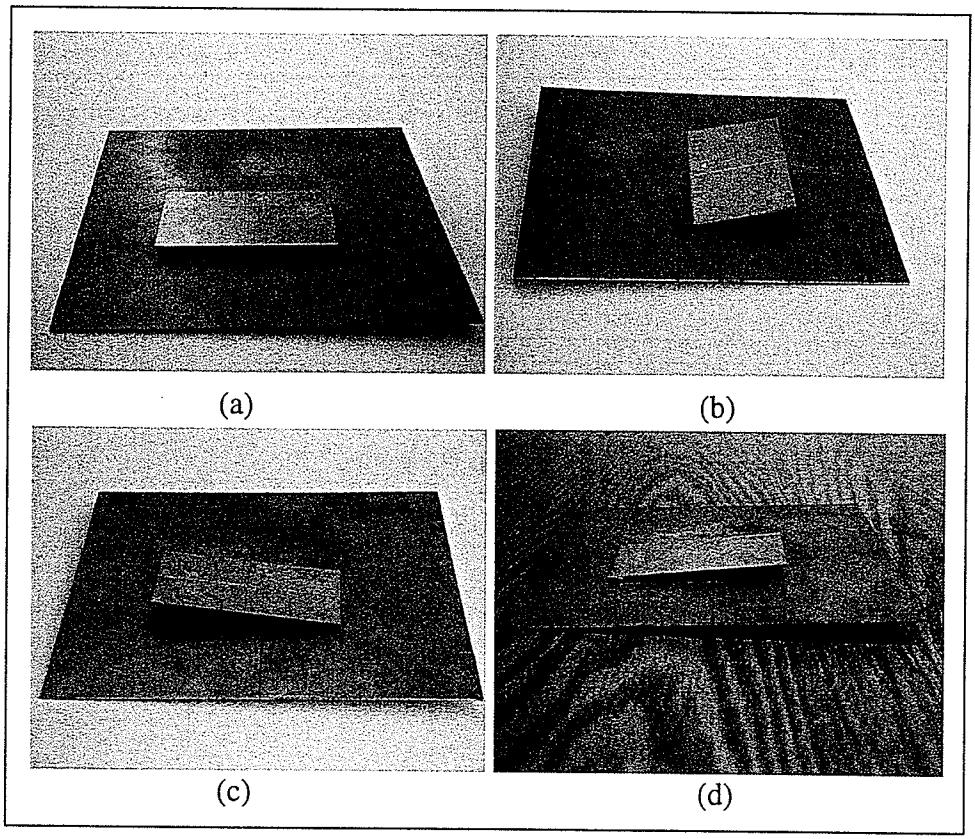

Figure 4.17: *Probe-fed MPA in its (a) original, (b) front, (c) right, and (d) left position.*

The S_{11} results measured for the antenna at different positions are shown in Figure 4.18. The different tilting position all seem to influence the matching, where the left tilt position provides the worst amount of matching at 2 GHz.

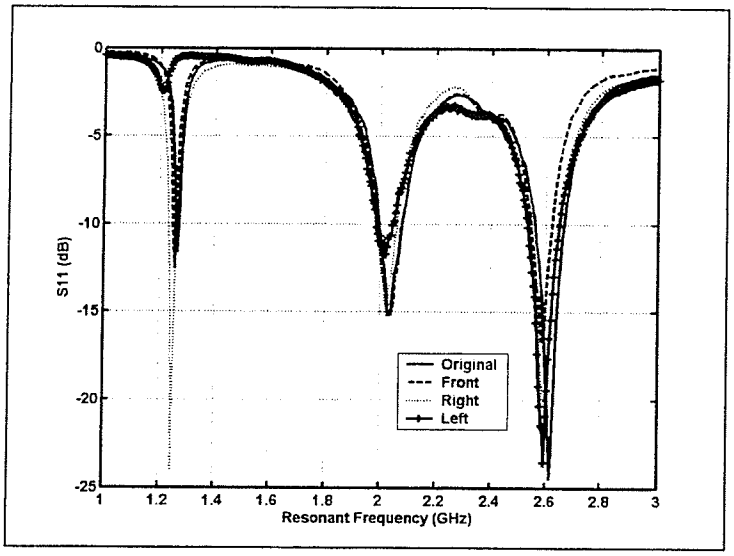

Figure 4.18: *Measured S_{11} results for the 2 GHz antenna at several positions.*

4.3.3 Finite Ground Plane

In the analysis and design of the antenna, including modelling the antennas in Ensemble, the size of the ground plane was always assumed to be infinite. However, since space is at a premium in most communications applications, a practical fabricated antenna has a finite ground plane. In the bulk-machined model, the ground plane size extends past the 18.9 GHz antenna by only 1.15λ, and its thickness is about 5 cm (7λ).

A finite ground plane gives rise to diffraction of radiation from the edges of the ground plane resulting in changes in radiation pattern, and radiation conductance [11]. According to research done by Huang [4], a finite ground plane induces ripples in the E-plane and gives rise to scattered radiation in the backward direction. Furthermore, Noghanian reported that by increasing the ground plane radius, the gain increases while the E-field's main beam becomes narrower with less back radiation. The ground plane's

increased thickness (past 0.1λ) was also reported to influence the radiation pattern as shown in Figure 4.19.

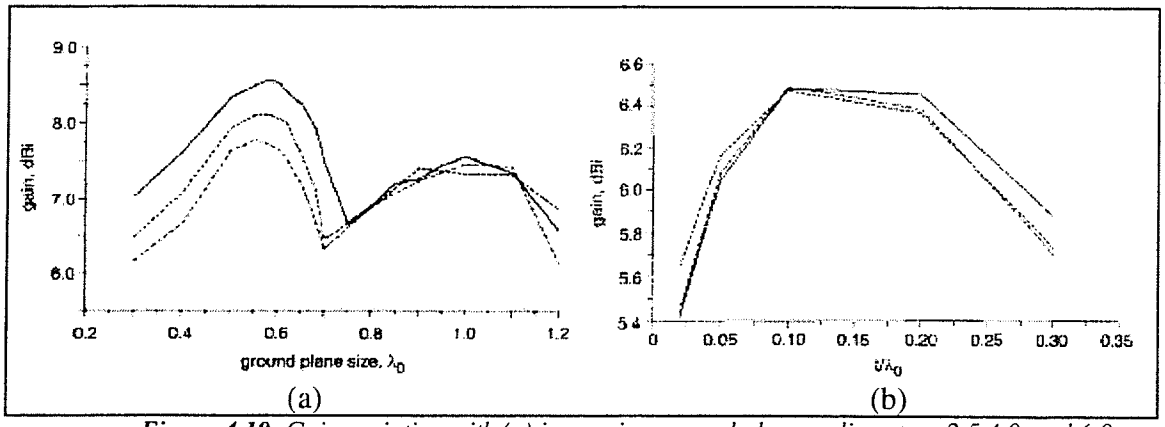

Figure 4.19: *Gain variation with (a) increasing ground plane radius at ε_r=2.5,4.0, and 6.0, and with (b) increasing ground plane thickness, t.*

Therefore, error sources and deviations such as Epoxy connection loss and a finite ground plane, lead to discrepancies between the theoretically predicted and measured results and may well account for the differences observed.

Chapter 5

Micromachined Model Fabrication and Results

The micromachined model's fabrication procedure and results are presented in this chapter. First, the design and construction of the corrugated membranes are described in detail. The corrugated membranes are then placed beneath the 18.9 GHz antenna, and the results obtained are given.

5.1 Corrugated Membrane Design and Fabrication Process

The square and circular corrugated membranes are designed for the maximum allowable deflection and flexibility, to achieve approximately the same amount of frequency shift obtained for the bulk-machined model within the first few hundred microns of air. The fabrication process consists of two main stages: the backside and frontside patterning and etching, achieved using standard bulk micromachining fabrication methods described in Section 2.2.

5.1.1 Membrane Design

The first stages of design require the design of lithographic masks using Adobe Illustrator 10.0. For optimum printing and feature quality, the micromachined corrugated membranes are designed with a resolution of 56 μm, exceeding the printer resolution of 7 μm. The depth of the corrugations is set to 5 μm, as illustrated in the corrugation profile's cross-section in Figure 5.1.

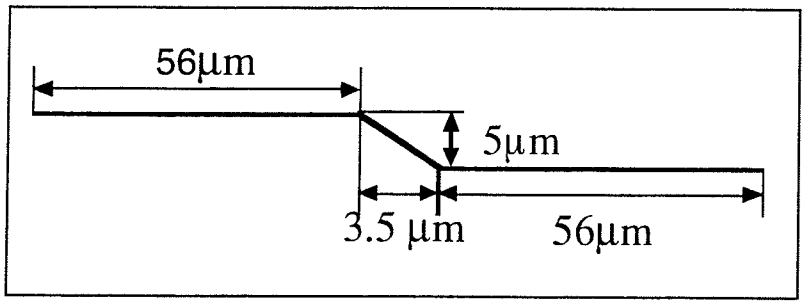

Figure 5.1: *Cross-section of the corrugation profile [7].*

Two sets of membranes, square and circular membranes were designed of varying sizes to view the effect of ground shape and size on the antenna's performance. The two sizes of diameter 10.34 mm and 9.22 mm are shown in Figure 5.2, in which the front side masks are to the right, and the backside masks are to the left. A 525 μm tolerance is given to the backside masks for over-etch and misalignment during lithography.

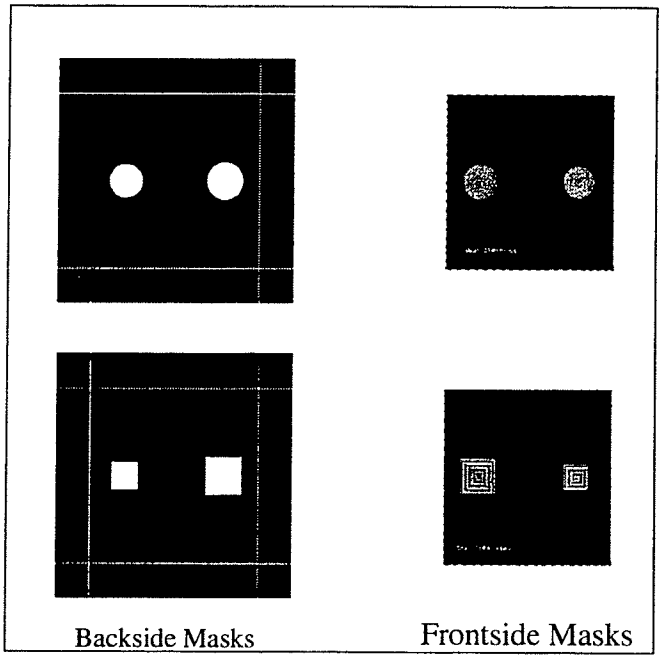

Figure 5.2: *Lithographic masks.*

The membrane outlines were positioned practically so that the two sizes can fit onto one wafer, and testing of either membrane can be accomplished by simply rotating the membrane wafer 180°C beneath the antenna.

5.1.2 Membrane Fabrication Process

A 400 μm thick <100> silicon wafer with 2 μm of wet thermal oxide was used for membrane fabrication. The fabrication process starts out with the backside patterning and etching, followed by the frontside patterning and etching.

5.1.2.1 Backside Patterning

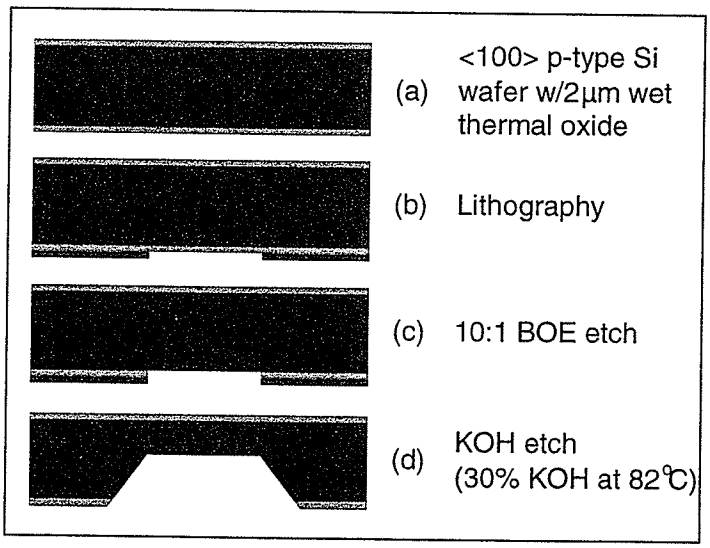

Figure 5.3: *Backside patterning and etching process.*

The wafer's front and backsides were first coated with photoresist. The front side was coated with a layer of resist to protect it when etching the backside. After spinning the resist on the wafer, it was soft baked at 110°C on a hot plate for 50 seconds. The wafer was then placed on an aluminum slab to cool for a few seconds.

The backside of the wafer was then aligned and patterned with the backside shadow mask illustrated in Figure 5.3(b). This process is also known as photolithography, in

which the UV light chemically develops the areas of the mask desired (in a positive resist, these are the areas that are shielded from the UV light). The chemically altered photoresist areas on the wafer were then rinsed off using developer solution. The wafers were then rinsed with de-ionized water and placed in the oven for a hard bake of the photoresist at 120°C for 20 minutes.

The wafer was then pulled out, wafer taped on the front as secondary protection to the front side of the wafer to prevent the resist on the front side from getting scratched off, The oxide layer was etched away on the backside by placing the wafer in a 10:1 BOE (buffered oxide etch) for 40mins. At this stage, the thickness of the wafer was measured to calculate the amount of time required to etch away the bulk of the wafer, leaving 5 μm for corrugation depth and 40 μm for a release etch. The measured thickness of the wafer was 416 μm, excluding the oxide layers thickness (4 μm). To allow for 5 μm for corrugation height etch, and to allow for a 40 nm release etch, the calculated thickness of the wafer to be etched is 366 μm. The etch rate of KOH for silicon is approximately 1.1 μm/minute, and thus the etch duration for the wafer is around 5.5 hours. Note that the front side is coated with oxide and is not completely etched away because KOH etches oxide at only 0.25 μm/hour.

5.1.2.2 Frontside Patterning

The backside of the wafer was coated with resist and soft baked, then hard baked for protection. The front side of the wafer was then coated with resist, soft baked, and patterned and developed, then hard baked for 20mins. Next, a BOE was done as in Figure 5.4(a), where the backside of the wafer was covered with wafer tape again as a secondary protection. Then the resist was rinsed off both sides using acetone, and the KOH etch was

performed for the front side corrugation features. A 20 nm adhesion layer of chrome and a 1.18 μm thick layer of copper were thermally evaporated on the frontside surface of the wafer. Before doing the XeF_2 release etch, a 5 seconds BOE was done to the wafer to remove any native oxide on the silicon surface.

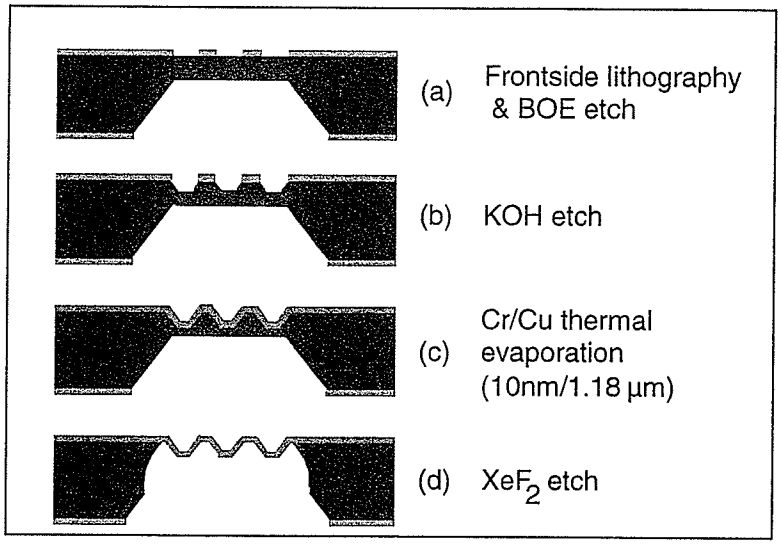

Figure 5.4: *Frontside patterning and etching process.*

5.1.3 Fabricated Membrane Results

There were two shapes of membrane designed and fabricated: square and circular membranes with diameters of 10.34 mm and 9.22 mm. The smaller membrane fits almost to the size of the patch element behaving like a finite ground plane, while the 10.34 mm membrane extends past the perimeter of the patch element by 1.30 λ. The results obtained when releasing these membranes are presented in this section.

The circular membranes were first released with a XeF_2 etch, and ruptured as soon as the etching process reached the 20 nm chrome layer. A few images of this damaged membrane taken at different magnifications are illustrated in Figure 5.5. In Figure 5.5(a) and (b), the membrane appears to be relaxed between four radial lines of

shear stress spread outward throughout the membrane. Looking more closely at the membrane's corrugations in Figure 5.5 (d), the corrugations were not etched along these four radial diagonals. Therefore, the shear stress along the surface of the membrane was not evenly distributed, resulting in the ripping of these membranes.

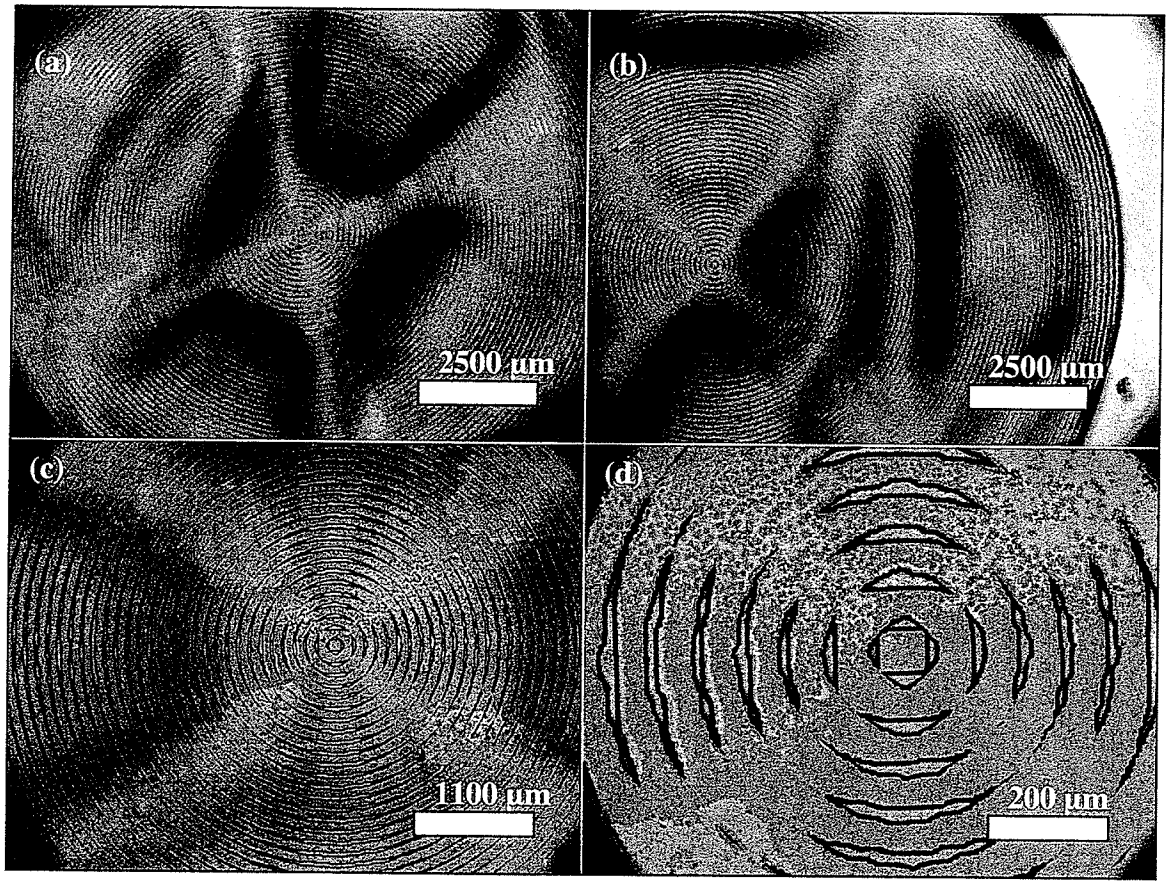

Figure 5.5: *Circular corrugated membrane images at: (a) 25x, (b) 25x, (c) 50x, and (d) 200x magnification.*

The square membranes were then released, and resulting images are shown in Figure 5.6. These membranes survived the release etch mostly because the majority of the corrugated features were successfully etched as illustrated in Figure 5.6(b). Therefore, the distribution of stress is more uniform along the surface of the square membranes.

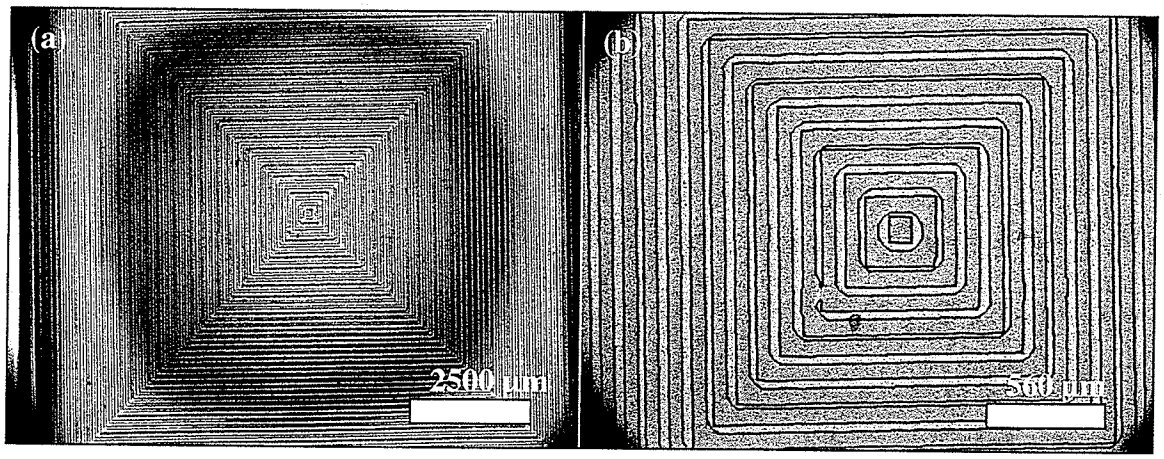

Figure 5.6: *Square corrugated membrane images at: (a) 25x, and (d) 50 x magnifications.*

These square membranes were then actuated to measure the amount of deflection achievable using the set-up below. A high-voltage source is connected to the membrane wafer via a probe, as illustrated in Figure 5.7. The wafer is held in place beneath the microscope using two pieces of glass. The aluminum plate beneath the membrane wafer is grounded.

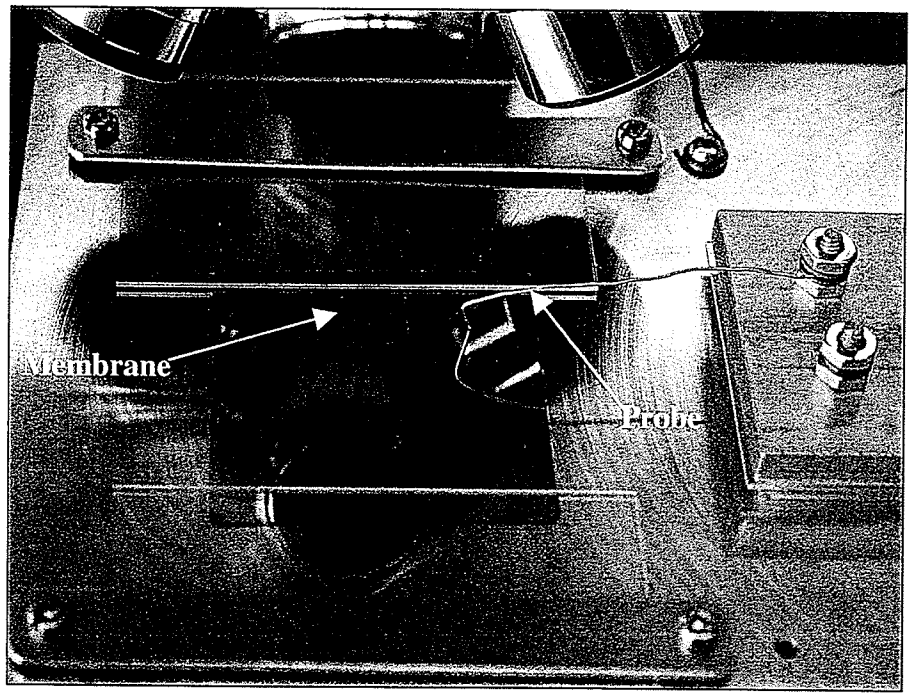

Figure 5.7: *Square membrane actuation set-up.*

The 10.34 mm membrane deflections were measured for applied voltages of up to 1000 volts. The testing did not exceed 1000 volts because of arching and shorting affects that may damage the membranes. The measured results are shown in Figure 5.8.

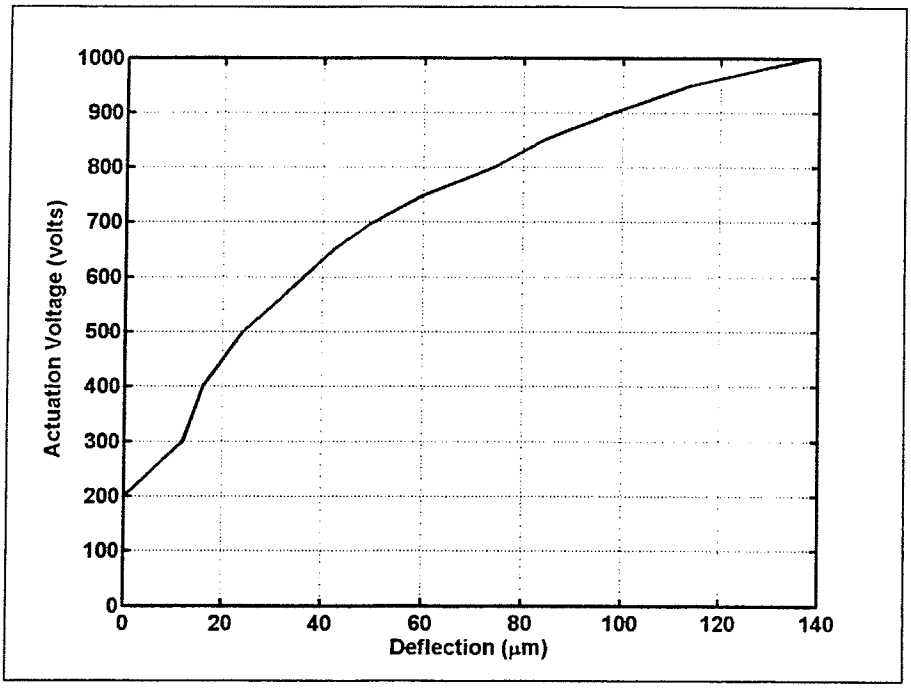

Figure 5.8: *The square membrane's deflection at its center measured with increasing voltage.*

The square membrane begins to deflect past 200 volts of applied voltage, and achieves a total deflection of 138 μm.

5.2 Micromachined Model Results

In the micromachined model, the 10.34 mm square membrane was placed beneath the 18.9 GHz antenna in a high frequency jig shown in Figure 5.9. The electrical connection from the probe to the membrane wafer is made by the means of pressure contact.

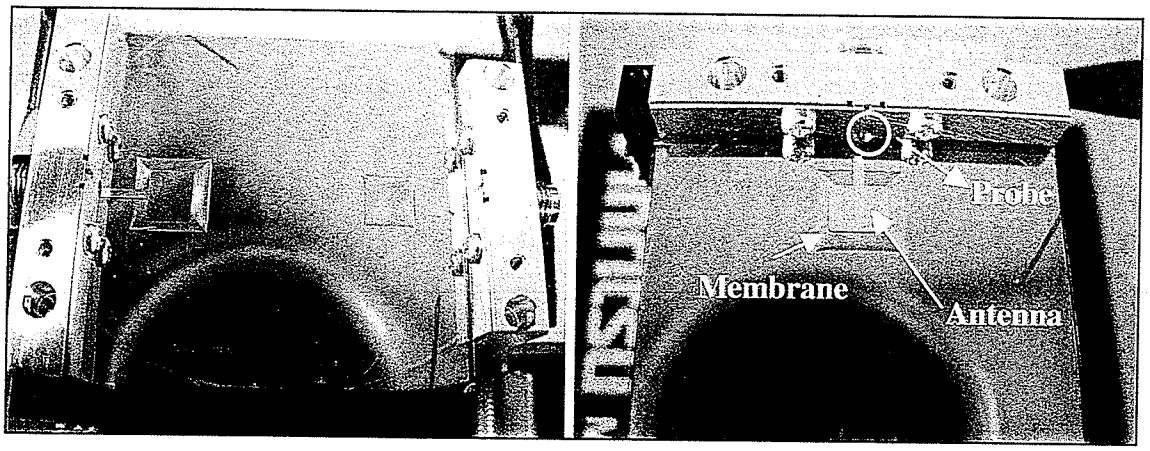

Figure 5.9: *Two views of the square membranes placed beneath the MPA.*

The 18.9 GHz MPA's copper thickness was set to 2.8 μm to reduce any skin depth losses, as observed in Section 4.3.1. The high-frequency jig was then connected to the network analyzer and to the high-voltage source for measurements, as shown in Figure 5.10.

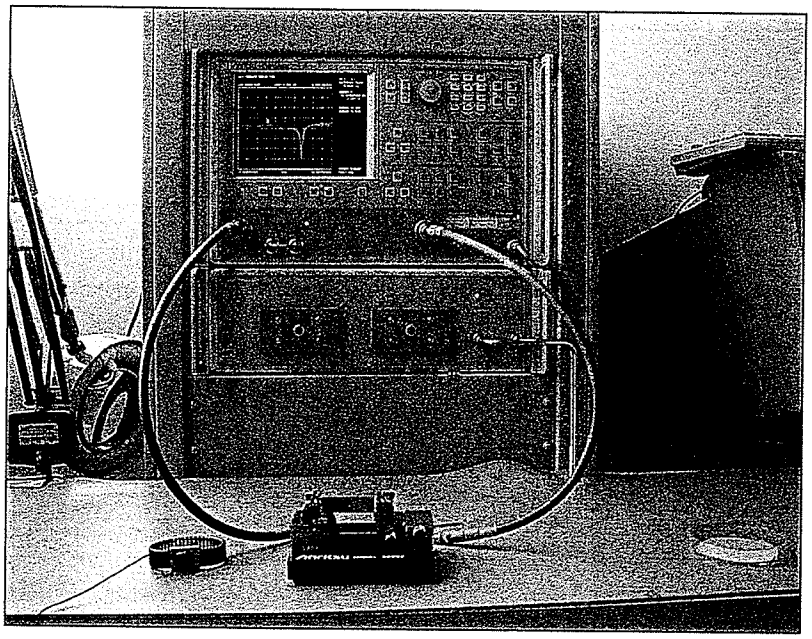

Figure 5.10: *Measurement set-up.*

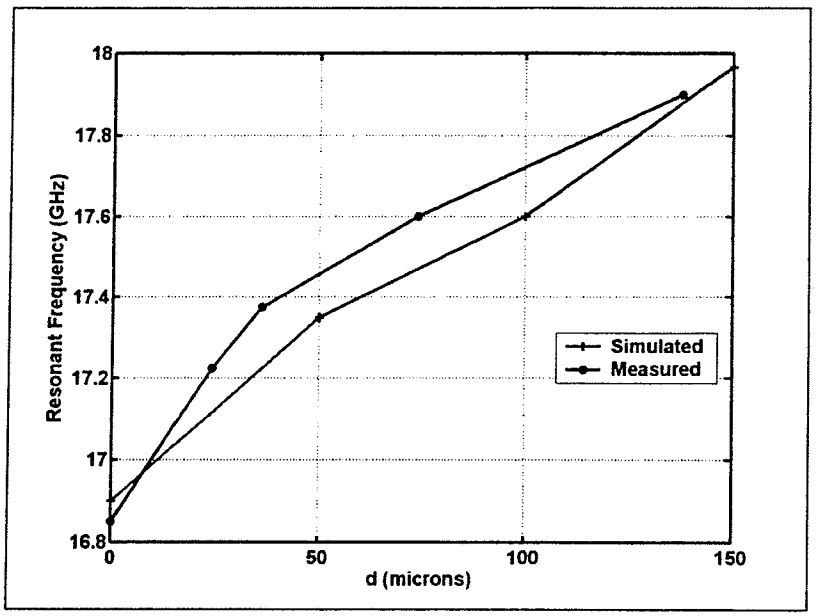

Figure 5.11: *Comparison of the 18.9 GHz antenna's Ensemble simulated and VNA measured resonant frequencies for varying air- gap heights.*

A comparison of the measured frequency shift obtained with the simulated frequency shift is shown in Figure 5.11. The measured results for the micromachined model are very similar to the simulated results in comparison to the results obtained for the bulk-machined model. For a very small change in air-gap height, approximately 138 μm, the micromachined model experienced a 1.05 GHz shift in frequency. For the simulated results, an air-gap height of 150 μm is necessary to experience a frequency shift of 1.066 GHz. Figure 5.12 illustrates the measured frequency shifts obtained for the micromachined model at different membrane deflections. The MPA's impedance bandwidth is shown in Figure 5.13 for a optimum matched impedance of 50 Ω. However, the impedance varies at different air-gap heights, ranging between 30 - 45.2 Ω. Therefore, a different approach is required to measure the impedance bandwidth using an average matched impedance of 37.6 Ω. The Smith charts measured at different voltages and deflections are included in the Appendix for reference.

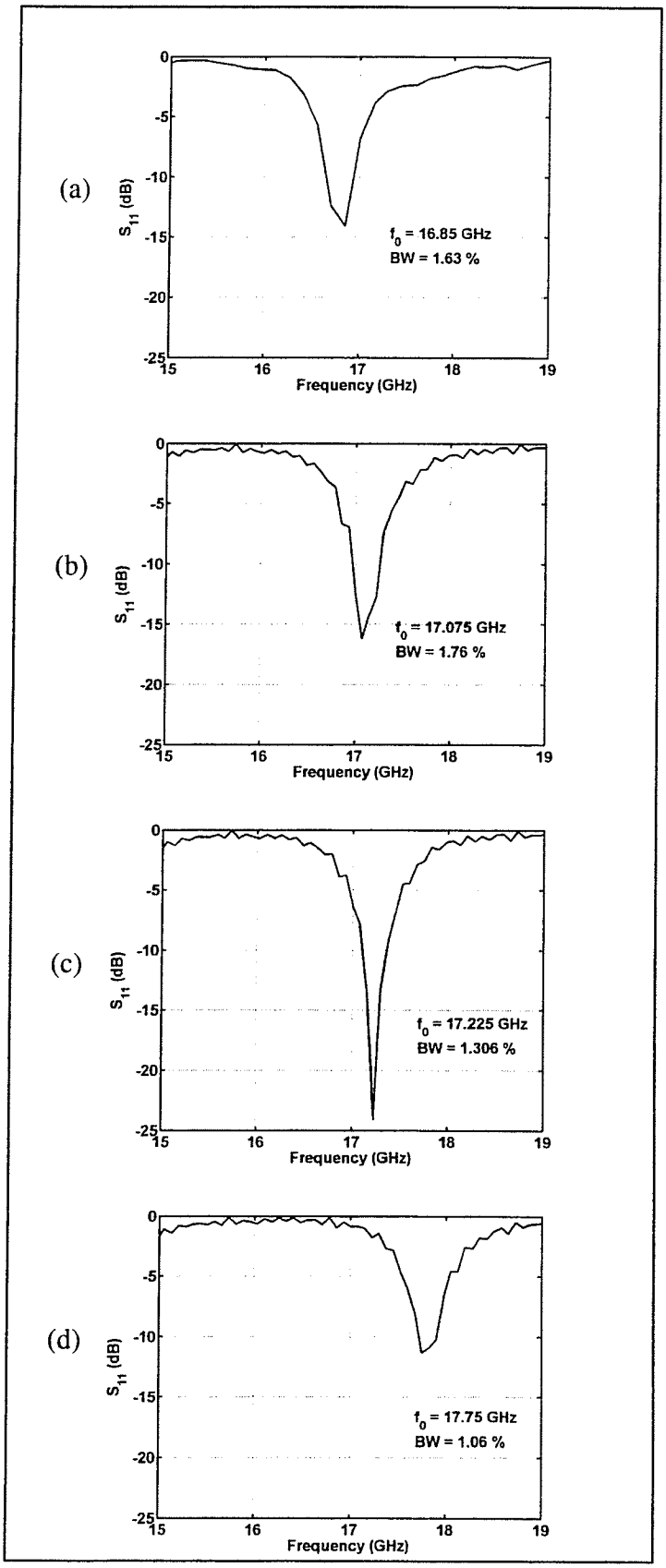

Figure 5.12: *Frequency shifts observed for S_{11} plots at deflections ranging from 0 μm up to 138 μm.*

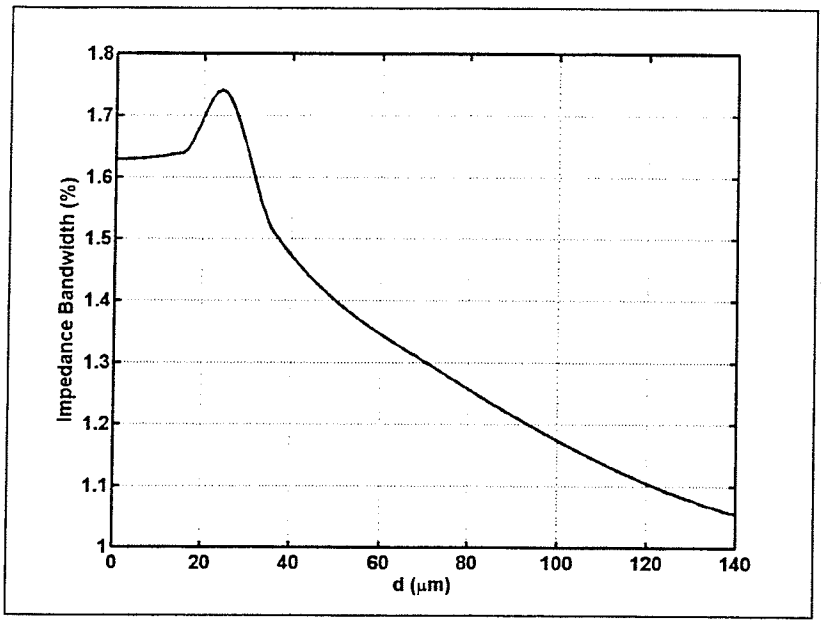

Figure 5.13: *Impedance bandwidth with increasing air-gap height.*

Table 5.1: *Simulated and measured frequency shift results for the 18.9 GHz antenna.*

	Simulated Results Frequency Shift (MHz)	**Measured Results Frequency Shift (MHz)**
138 μm Deflection		1050
150 μm Deflection	1066.7	

Chapter 6

Conclusion

6.1 Summary

In conclusion, a novel, frequency-tunable micromachined MPA is introduced in this thesis. Simulation results obtained confirmed predictions that introducing a variable air-gap beneath the MPA results in a frequency shift. The resonant frequency increased due to reduced effective permittivity. The bulk-machined model designed and tested for an 8.8 GHz and 18.9 GHz antenna achieved a frequency shift of 400 MHz for both antennas. The discrepancies present between the simulated and measured results are due to several sources of error and loss such as epoxy loss, non-parallel geometry, and ground plane size and thickness. For the micromachined model, the measured results were very similar to the simulated results with little discrepancy achieving, a frequency shift of 1.05 GHz. This antenna is useful for several applications, and can replace an array of antennas conserving space and cost.

6.2 Future Work and Recommendations

Future research is to implement this tunable MPA in a stacked-element configuration and analyze its performance. This arrangement may enhance the impedance bandwidth of the antenna, and reduce its fragility, making it easier to work with. An additional proposed study is to place parasitic elements along the perimeter of the MPA and examine their effects on the antenna's performance. The placement of these elements may enhance the impedance bandwidth and gain of the antenna.

APPENDIX

Smith Chart Data Comparison

Comparisons of the simulated and measured Smith charts for the 18.9 GHz antenna's bulk-machined and micromachined models with a 0.05 mm air-gap are presented. The impedance of the antenna at its resonant frequency ideally should appear close to the normalized r = 1 circle (i.e. the 50 Ω circle), thereby matching to a typical 50 Ω SMA connector, and minimizing reflections. Figure 1 shows the simulated Smith chart, where the impedance is 53.7 + 0.2j Ω at the resonant frequency. In Figure 2, the bulk-machined model's impedance is 70 – 25j Ω, a poorer match. The micromachined model's impedance is better than the bulk-machined model at 37 + 2j Ω.

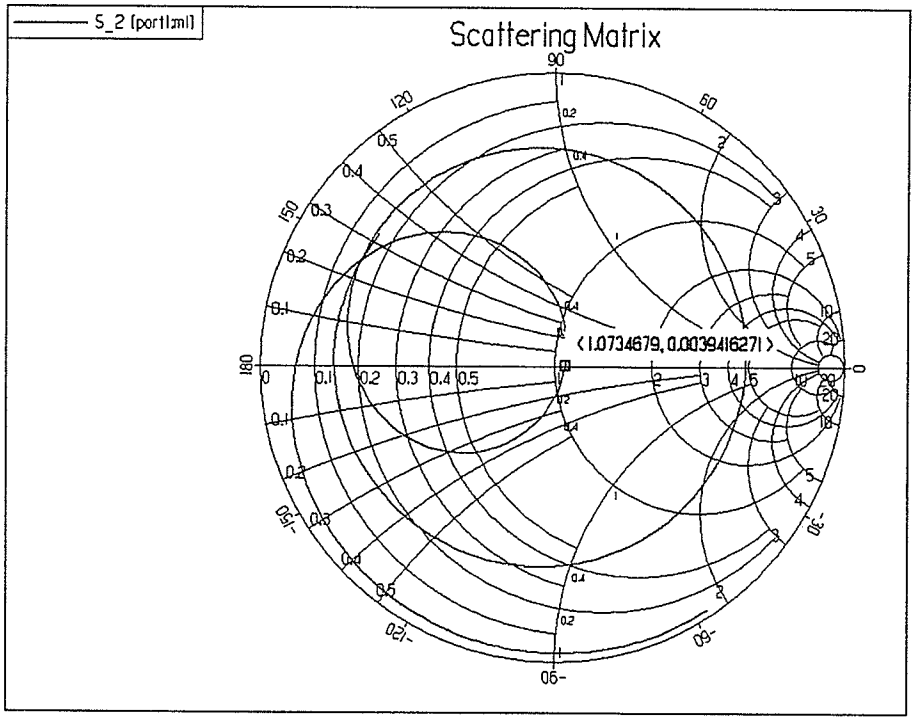

Figure 1: Simulated Smith Chart.

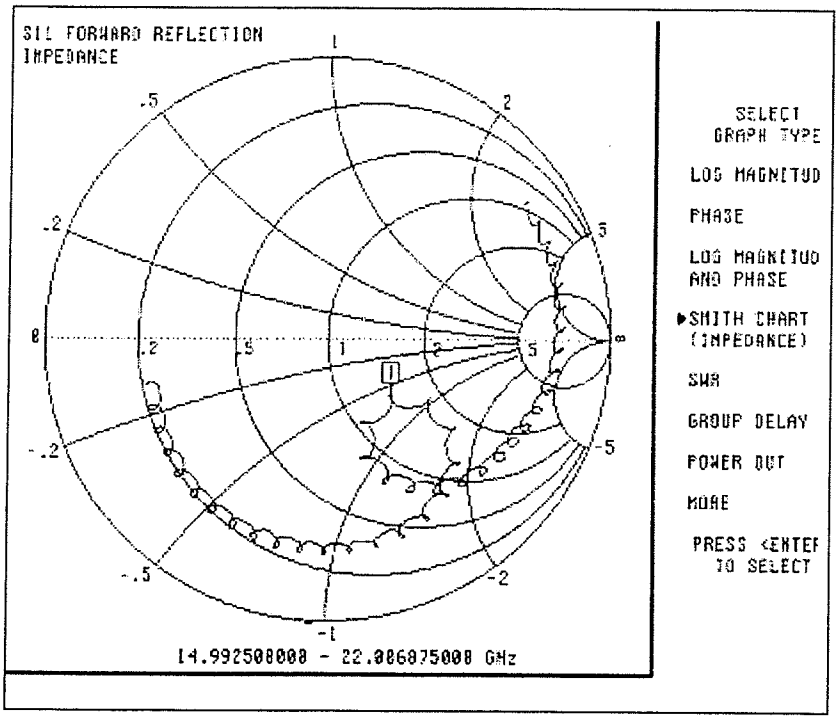

Figure 2: *Bulk-machined model's measured Smith Chart.*

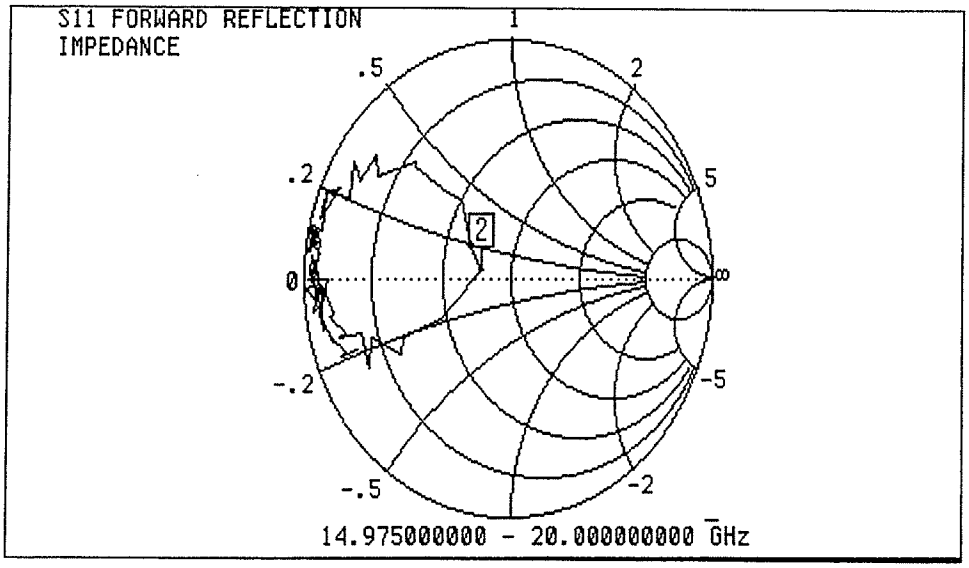

Figure 3: *Micromachined model's measured Smith Chart.*

Smith charts for the micromachined model antenna are shown in Figures 4, 5, 6 and 7 for increasing air-gap heights ranging from 0 μm to 138 μm. The antenna's impedance at resonant frequency varies between 30 Ω to 45.2 Ω, and is closest to an optimum 50 Ω impedance match at an air-gap height of 25 μm.

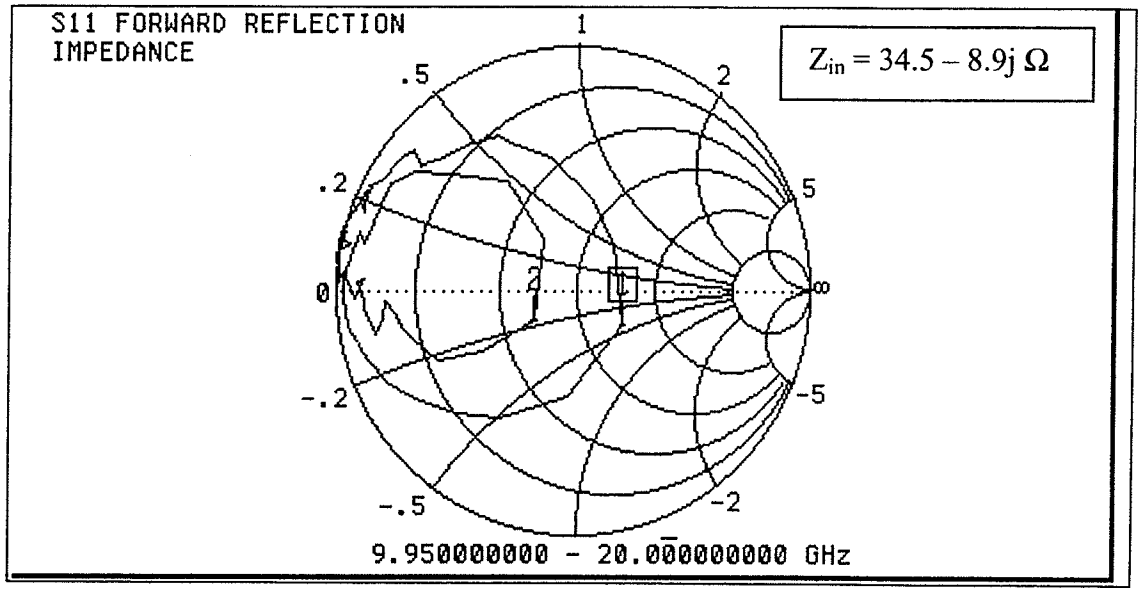

Figure 4: *Micromachined model's Smith chart at 0 volts (0 μm deflection).*

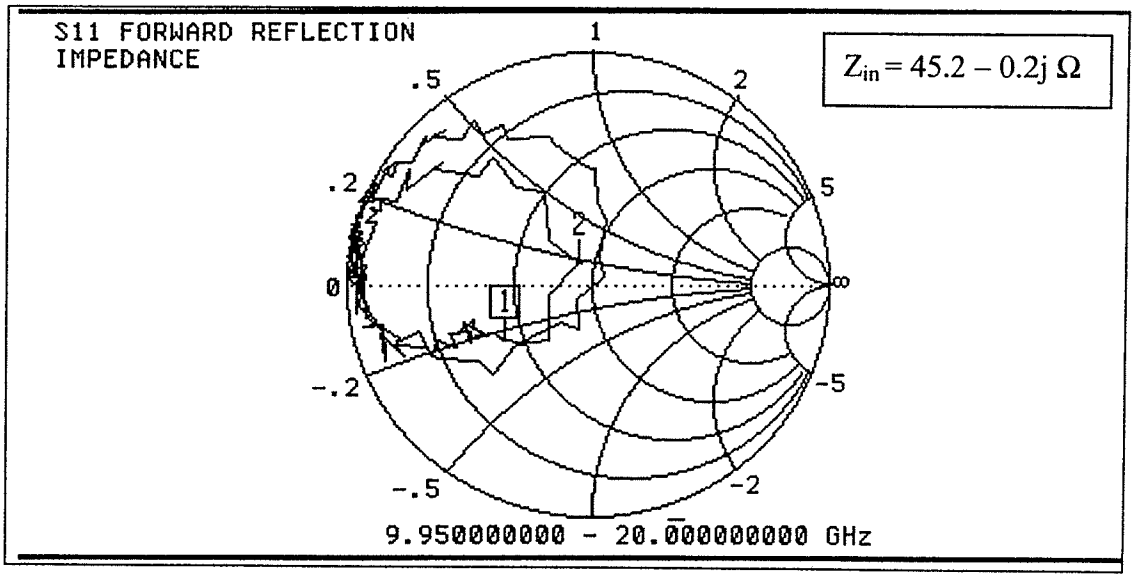

Figure 5: *Micromachined model's Smith chart at 500 volts (25 μm of deflection).*

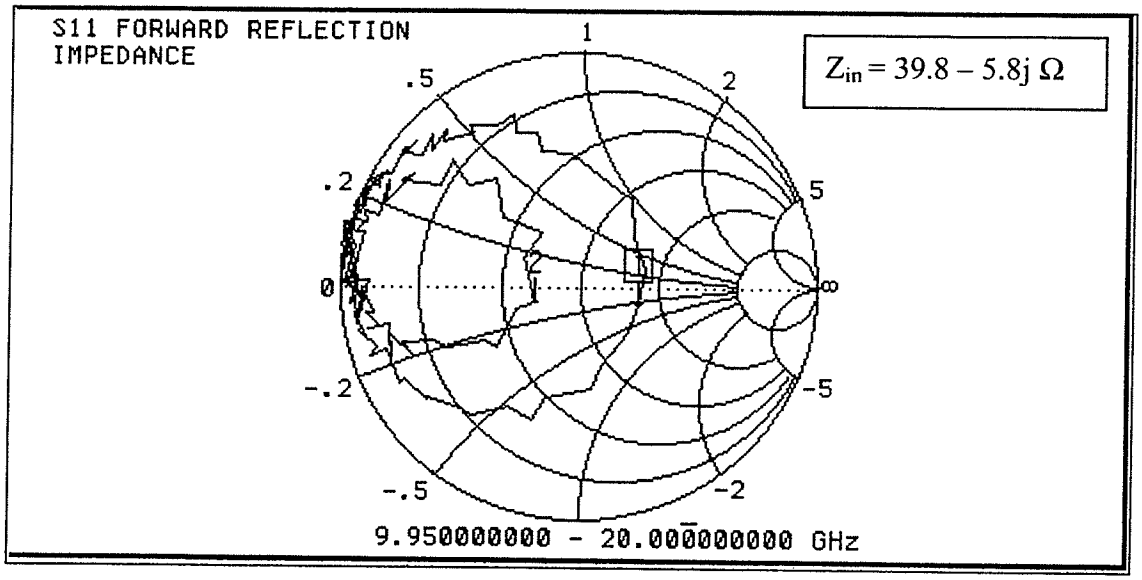

Figure6: *Micromachined model's Smith chart at 600 volts (38 μm of deflection).*

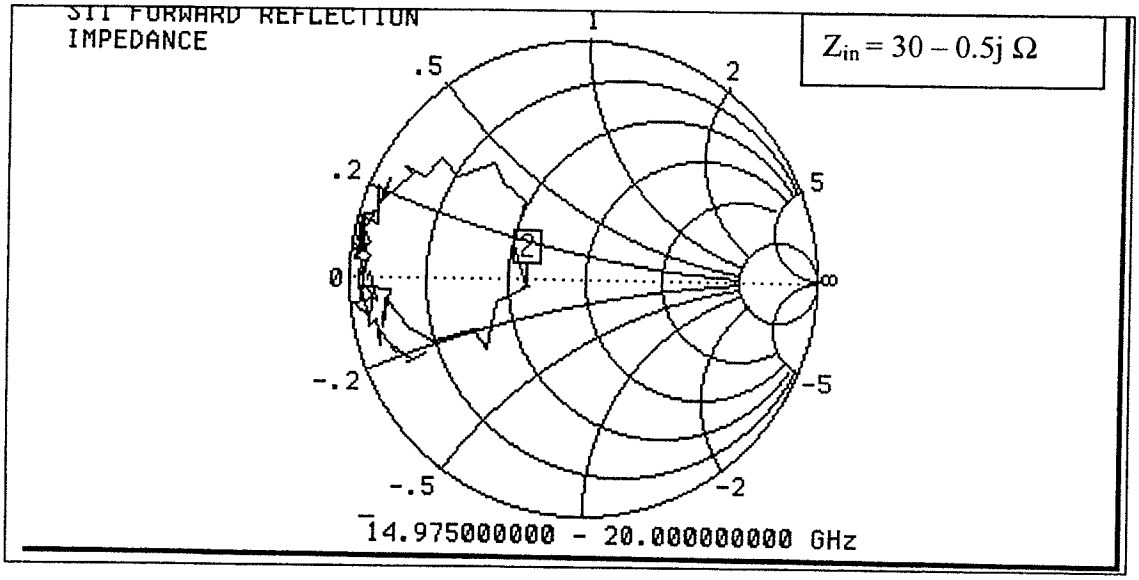

Figure 7: *Micromachined model's Smith chart at 1000 volts (138 μm of deflection).*

REFERENCES

(1) C. Balanis, "Antenna Theory: Analysis and Design". Arizona State University. John Wiley and Sons Inc. 2nd Edition, 1997.

(2) J.R. James, P.S. Hall, " Handbook of Microstrip Antennas", Vol. 1 &2, Peter Peregrinus Ltd., London, United Kingdom, 1989.

(3) Dahele, J.S., Lee, K.F., "Theory and experiment on microstrip antennas with air-gaps", IEEE Proceedings, Vol.132, Pt.H, No.7, December 1985.

(4) R. Garg, P. Bhartia, P., Bahl, I, "Microstrip Antenna Design Handbook," Archtech House, Inc., 2001.

(5) Kovacs, G. T.A., Micromachined Transducers Sourcebook, The Mc-Graw-Hill Companies Inc., 1998.

(6) MEMS Guide. May 14, 2003.
< http://www.memsguide.com/MEMSequipments-Micromachining_bulk.htm >.

(7) Chrusch, D., "Corrugated Micromachined Membrane Structures", Proceedings of the IEEE Canadian Conference on Electrical and Computer Engineering, August 2002, pg. 445 - 449.

(8) Jerman, J. H., "The Fabrication and use of micromachined corrugated silicon diaphragms", Sensors and Actuators, vol. A21-A23, 1990, pg. 988 - 992.

(9) Ansoft Corporation. May 21st, 2003. "Ensemble Essentials."
< http://www.ansoft.com/workshops/hfworkshop02/Ensemble_Essentials.pdf >.

(10) Noghanian, S., and Shafai L., "Control of microstrip antenna radiation characteristics by ground plane size and shape," IEE Microwave Antennas Propagation, vol. 145, no: 3, pp. 207 - 212, June 1998.

(11) G.H. Huff, and J.T. Bernhard, "Improvements in the Performance of Microstrip Patch Antennas on Finite Ground Planes Through Ground Plane Edge Serrations," IEEE Microwave and Wireless Component Letters, vol. 12, no. 8, pp. 308 - 310, August 2002.

(12) Bhartia, P., and Bahl, I., "A Frequency Agile Microstrip Antenna", IEEE AP-S International Symposium Digest, 1982, pp.304-307.

(13) Moosavi, P., and Shafai L., "Directivity of Microstrip Ring Antennas and Effects of Finite Ground Plane on the Radiation Parameters", IEEE Proceedings, 1998, pp. 672 – 675.

(14) Bernhard, J.T., Kiely, E., and Washington, G., "A Smart Mechanically Actuated Two-Layer Electromagnetically Coupled Microstrip Antenna with Variable Frequency, Bandwidth, and Antenna Gain", IEEE Transactions on Antennas and Propagation, Vol. 49, No. 4, pp. 597 – 601, April 2001.

(15) Gauthier, G. P., Raskin, J., Katehi, L.P.B., Rebeiz, G.M., "A 94-GHz Aperture-Coupled Micromachined Microstrip Antenna", IEEE Transactions on Antennas and Propagation, Vol. 47, No. 12, pp. 1761 – 1766, December 1999.

(16) Papapolymerou, I., Drayton, R.F., Katehi, L.P.B., "Micromachined Patch Antennas", IEEE Transactions on Antennas and Propagation, Vol. 46, No. 2, pp. 275 – 283, February 1998.